The Catalytic Degradation of Carbon Nanomaterials

by

Philip Michael Fournier

B.S. Florida State University, 2011

Submitted to the Graduate Faculty of the

Kenneth P. Dietrich School of Arts and Sciences in partial fulfillment

of the requirements for the degree of

Master of Sciences

University of Pittsburgh

2016

UNIVERSITY OF PITTSBURGH

Kenneth P. Dietrich School of Arts and Sciences

This thesis was presented

by

Philip Fournier

It was defended on

May 27, 2016

and approved by

Haitao Liu, Assistant Professor, Department of Chemistry

Jill Millstone, Assistant Professor, Department of Chemistry

Thesis Director: Alexander Star, Professor, Department of Chemistry

The Catalytic Degradation of Carbon Nanomaterials

Philip Fournier, M.S.

University of Pittsburgh, 2016

The explosion of research into carbon-based nanomaterials has been driven by their possible application to a wide range of fields. While materials such as graphene and cellulose nanostructures show great potential due to their physical qualities, understanding of their stability and toxicity is still not well-defined. This report explores the result of exposing new and familiar nano-sized carbon architectures to oxidative environments, with the intent of furthering the safe and effective implementation of them. First, intentional degradation of graphene oxide is exhibited through the use of iron oxide nanoparticles as a component in the Fenton reaction. Next, the morphologies of different nanocellulose sources are thoroughly characterized using microscopy techniques. The interaction between myeloperoxidase and one of these nanocellulose samples, which results in acute aggregation, is then investigated. An additional degradation system utilizing DNA origami and horseradish peroxidase is also introduced as a possible approach for graphene oxide degradation. Finally, two emerging nanomaterials, carbon nanofibers and chitin, are analyzed and their pulmonary toxicity assessed in collaboration with the National Institute of Occupational Safety and Health.

TABLE OF CONTENTS

LIST OF TABLES

LIST OF FIGURES

LIST OF ABBREVIATIONS

AFM – atomic force microscopy

APTES – (3-aminopropyl)triethoxysilane

AVAP – American value added pulping

CCG – chemically converted graphene

CNC – nanocrystalline cellulose

CNT – carbon nanotubes

DLS – dynamic light scattering spectroscopy

EDC – N-(3-dimethylaminopropyl)-N'-ethylcarbodiimide hydrochloride

EDX – energy-dispersive X-ray spectroscopy

GO – graphene oxide

HEPES – 4-(2-hydroxyethyl)-1-piperazineethanesulfonic acid

HGO – holey graphene oxide

HRP – horseradish peroxidase

MPO – myeloperoxidase

MWNT – multi-walled carbon nanotube

NC – nanocellulose

NCF – nanofibrillated cellulose

NHS – N-hydroxysuccinimide

NIOSH – National Institute for Occupational Safety and Health

NP – nanoparticle

PAH – polycyclic aromatic hydrocarbon

PBS – phosphate buffered saline

PVP – polyvinylpyrrolidone

RGO – reduced graphene oxide

SDS – sodium dodecyl sulfate

SEM – scanning electron microscopy

SWNT – single-walled carbon nanotube

TEM – transmission electron microscopy

UA – uranyl acetate

VGCNF – vertically grown carbon nanofiber

1.0   INTRODUCTION

Carbon nanomaterials have garnered a tremendous amount of research interest due to their unique physical and chemical properties. This fact is exemplified by the 50,000 research articles that have been published containing "graphene" in the title (according to Web of Science). Much effort has been invested into increasing the efficiency for the synthesis of these materials, as well as exploring the emergent properties for hybrid materials that utilize carbon nanostructures. However, the stability of materials such as graphene and cellulose nanocrystals in a variety of environments will dictate their toxicity, manipulation and application. The degradation of carbon nanomaterials may be a desired property that allows for their implementation in biological systems, while controlled decomposition may be usefully exploited to prepare "holey" 2-D structures. An enhanced understanding of the degradation of nanomaterials such as graphene and nanocellulose will lead to a safer and more effective implementation of these exciting and novel structures.

1.1   GRAPHENE AND GRAPHENE OXIDE

Carbon exists in a number of different bonding arrangements, and the differing properties of these allotropes make elemental carbon a highly versatile and unique building block for creating novel materials. At the nanoscale, whereby at least one dimension of the material is between 1 – 100 nm, a multitude of carbon-based structures are found. The sp^2 hybridization of carbon atoms, which allows for extended π-conjugation and results in unique physical and chemical properties, is seen for 0-D (fullerenes), 1-D (nanotubes), and 2-D (graphene) nanomaterials.[1] Since the first isolation of graphene by Novoselov and coworkers,[2] investigation of this material has revealed a number of unprecedented qualities, such as tensile strength (130 GPa) and Young's modulus (1 TPa).[3] The structure of graphene can be viewed as the parent of other sp^2 forms of carbon, as shown in Figure 1.
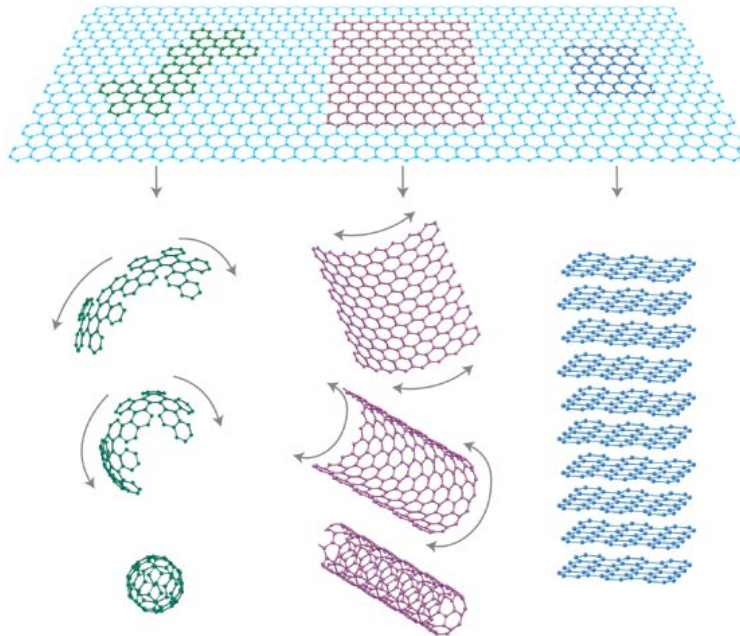
Figure 1: Graphene and related structures

Figure 1: Graphene and its structural relationship to fullerenes, single-walled carbon nanotubes, and graphite; adapted from [1].

While non-modified or "pristine" graphene has been extensively studied and shown to have extraordinary properties, the stability of graphene in various environmental conditions will ultimately decide how this material can be utilized. The formation of defects in graphene under certain conditions creates a novel and interesting derivative known as holey graphene.[4] A number of different approaches have been taken to produce holey graphene, all utilizing oxidizing environments such as nitric acid,[5] or oxidation catalysts like enzymes[4] and metal nanoparticles.[6, 7] The result of all these techniques is the introduction of defect sites in the basal plane of the graphitic sheet, as shown in Figure 2.
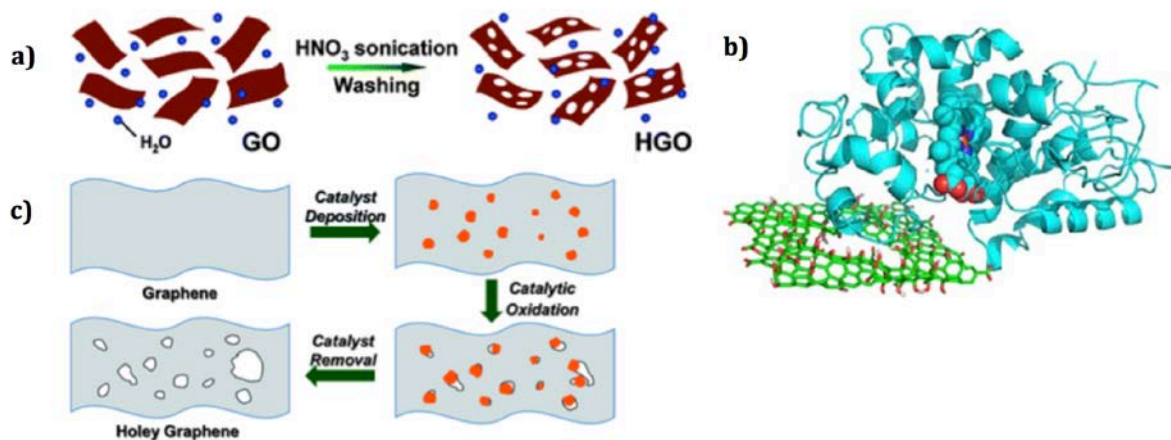
Figure 2: Defect formation in 2-D carbon nanomaterials

Figure 2. Holey graphene preparation routes, using a) HNO_3, adapted with permission from [5]; Copyright 2011 American Chemical Society, b) horseradish peroxidase and H_2O_2 (adapted) with permission from [4]; Copyright 2011 American Chemical Society, and c) Ag nanoparticles (adapted from [6]).

Graphene oxide (GO), a graphene derivative that includes a number of different oxygen-containing moieties, is commonly used in the formation of holey graphene due to its ease of preparation and aqueous colloidal stability. Most preparations of GO are based on a protocol first

3

published by Hummers and Offeman,[8] which uses strong oxidizing agents to functionalize graphite with carbonyl, carboxylic acid, epoxy, and hydroxyl functional groups. Exfoliation causes the separation of graphite oxide into individual planes, forming graphene oxide. Facile reductive treatments of GO allow for the recovery of some graphene qualities. The scheme for producing reduced GO (RGO), also known as chemically converted graphene (CCG), starting from graphite, is outlined in Figure 3.[9]
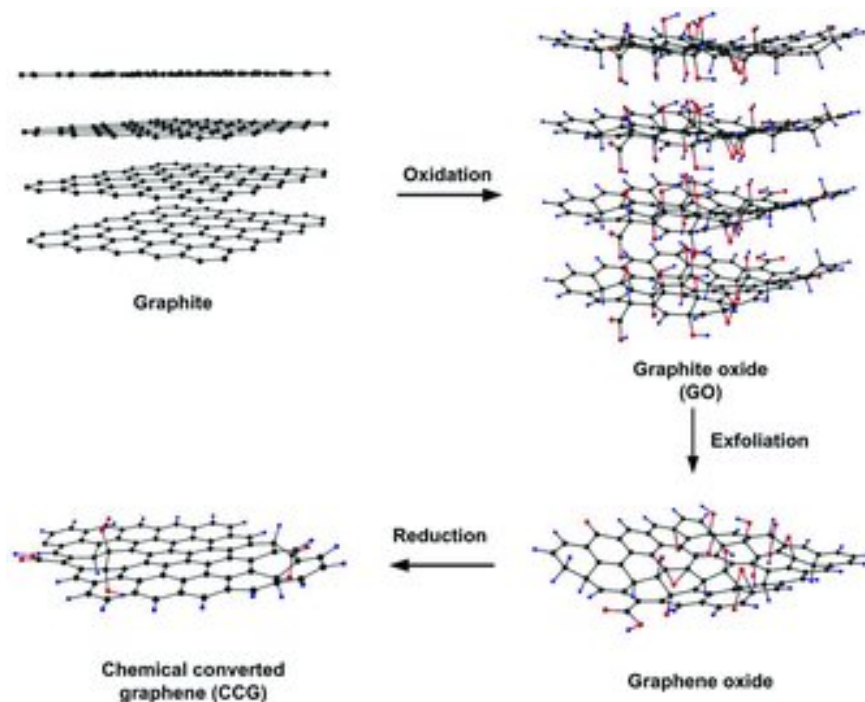
Figure 3: Preparation of GO and RGO

Figure 3. Scheme for the production of graphite oxide, GO, and RGO (or CCG) from graphite; adapted from [9].

The Fenton reagent,[10] which consists of Fe^{2+} and Fe^{3+} ions, H_2O_2, and an acidic aqueous environment, has been shown to be effective in the removal of polycyclic aromatic hydrocarbons from wastewater and contaminated soil.[11] While still debated, the degradation of

these contaminants is generally considered to be the result of oxidizing radicals produced by the reaction of iron ions with hydrogen peroxide, as shown in equations (1) and (2).

$$Fe^{2+} + H_2O_2 \rightarrow Fe^{3+} + OH^- + OH^{\bullet} \qquad (1)$$

$$Fe^{3+} + H_2O_2 \rightarrow Fe^{2+} + OOH^{\bullet} + H^+ \qquad (2)$$
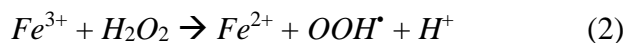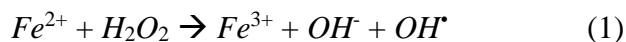
The addition of UV radiation to the reaction solution improves the efficiency of the Fenton system, as another pathway for the reduction of Fe^{3+} to Fe^{2+} is available.[12]

$$Fe^{3+} + H_2O_2 + h\nu \rightarrow Fe^{2+} + OH^{\bullet} + H^+ \qquad (3)$$
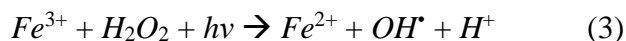
The radicals formed in equations (1-3) subsequently mineralize the polycyclic aromatic hydrocarbons (PAHs) into CO_2 and H_2O through hydrogen abstraction and addition reactions, which preferentially attack alcohol and olefin functionalities, respectively. [13] Reaction mechanisms for the interaction between hydroxyl radicals and organic groups found in PAHs are outlined in Figure 4.
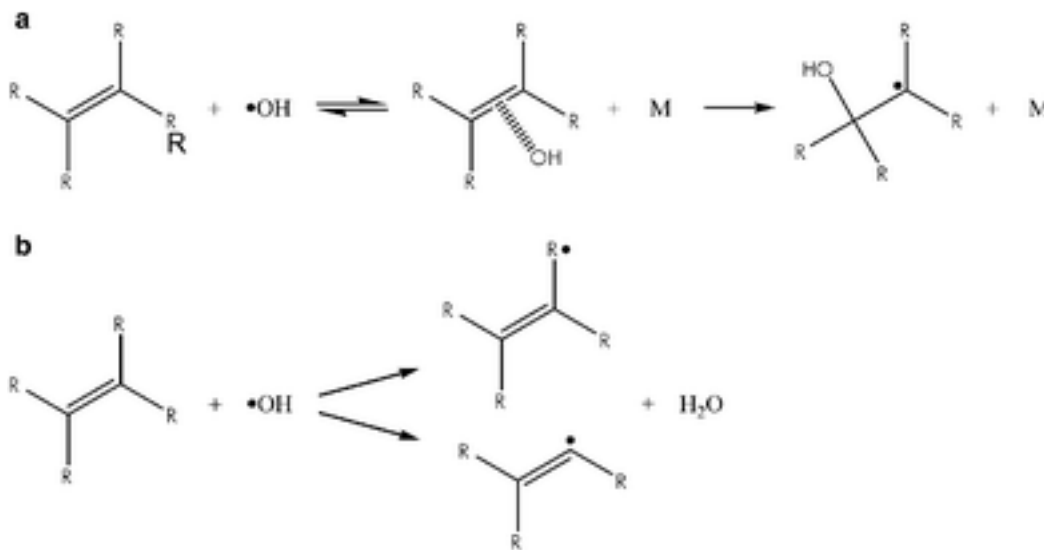
Figure 4: Defect-forming reactions in PAHs

Figure 4. Hydroxyl radical attack of organic compounds through a) addition and b) hydrogen abstraction; adapted from [13].

Graphene oxide has been used as a support substrate in peroxide-containing aqueous systems by multiple research groups,[14, 15] exhibiting GO's utility as a scaffold for Fenton catalysts. The applicability of GO, however, is questionable based on its susceptibility to the reactivity of hydroxyl radicals. It has been shown by Bai *et al.* that GO forms an increasingly holey and degraded structure when subjected to photo-Fenton conditions, eventually breaking down into graphene quantum dots after 3 days.[16] Degradation may be even more amplified when heterogeneous photo-Fenton catalysts employ nanoparticles, which show an increase in reactivity as a consequence of their enhanced surface energy. For example, the production of hydroxyl radicals was found to be at least 50-fold more effective at the catalytic sites for α–Fe_2O_3 and Fe_3O_4 nanoparticles than for dissolved Fe^{2+} ions.[17] This increase in activity would likely preclude the use of GO as a support substrate when the heterogeneous nanoparticle-GO architecture must be maintained. On the other hand, it is possible that this reactivity may be manipulated to create holey graphene structures. Such an application has already been demonstrated by Radich and Kamat, who used Au nanoparticles and RGO mixtures in a photo-Fenton environment to introduce well-defined holes into GO sheets.[7] Recently, TiO_2 nanoparticles were shown to be capable of forming holes in the basal plane of RGO through the production of hydroxyl radicals *via* a photocatalytic reaction.[18] The improved permeability of RGO to ions or electrolytes through the addition of holes is suggested by the authors to expand the applicability of TiO_2/GO nanocomposites in the fields of energy storage/conversion, where materials that allow for the transport of reactants at the electrode surface are required.

The stability and kinetics of the hydroxyl radical must first be considered before attempting to exploit it for deliberate degradation applications. Using the Stokes-Einstein

equation, the diffusivity (D) of a particle through a liquid can be calculated from the radius of the

particle (r), the temperature of the system (T), and the viscosity of the medium (η):[19]

$$D = \frac{k_B T}{6\pi\eta r} = \frac{(1.381\times10^{-23}m^2\cdot kg\cdot s^{-2}\cdot K^{-1})\cdot 298K}{6\pi(10^{-3}kg\cdot m^{-1}\cdot s^{-1})(42.85\times10^{-12}m)} = 4.56\times10^{-9}\ m^2 s^{-1}$$

where k_B is Boltzmann's constant. The radius is estimated using half of the O-H bond length.[20]

The lifetime (t) of this highly reactive species has been reported as 10^{-9} s,[21] which can be used

with the diffusivity to predict the displacement in 3-D:[22]

$$\left\langle (\mathbf{r}_N)^2 \right\rangle = 6Dt = 6\cdot 4.56\times10^{-9}m^2 s^{-1}\cdot 10^{-9}s = 2.74\times10^{-17}m^2\cdot\left(\frac{10^9 nm}{1\ m}\right)^2 = 27.4\ nm^2$$

Therefore, the maximum diffusion distance for a hydroxyl radical in water at room temperature

is less than 30 nm. Any degradation of a substrate, such as GO, should be within 27.4 nm of the

formation site, *i.e.* the nanoparticle surface.

Diffusion of the nanoparticle and hence diffusion of the reactive site for hydroxyl radical

formation will likely cause degradation across multiple locations on the GO sheet. Such diffusion

can be mitigated by anchoring the nanoparticle to a single site. Covalent coupling of the

nanoparticle to GO can be accomplished by utilizing coupling reactions between chemical

functional groups on the GO sheet and the nanoparticle surface. For example, He *et al.* have

shown that amine-functionalized Fe_3O_4 NPs and GO sheets are covalently linked *via* the

formation of an amide bond between carboxylic acid functional groups on GO and amine

functional groups on the Fe NP.[23] The reaction scheme is given in the Figure 5. The first step

involves the reaction of the carboxylic acid group with N-(3-dimethylaminopropyl)-N'-

ethylcarbodiimide hydrochloride (EDC), which forms an unstable intermediate. The stability is

enhanced by the use of N-hydroxysuccinimide (NHS) and allows for the storage of this material.

Finally, the reaction between the primary amine on the Fe NP and the carboxylic carbon forms an amide bond.
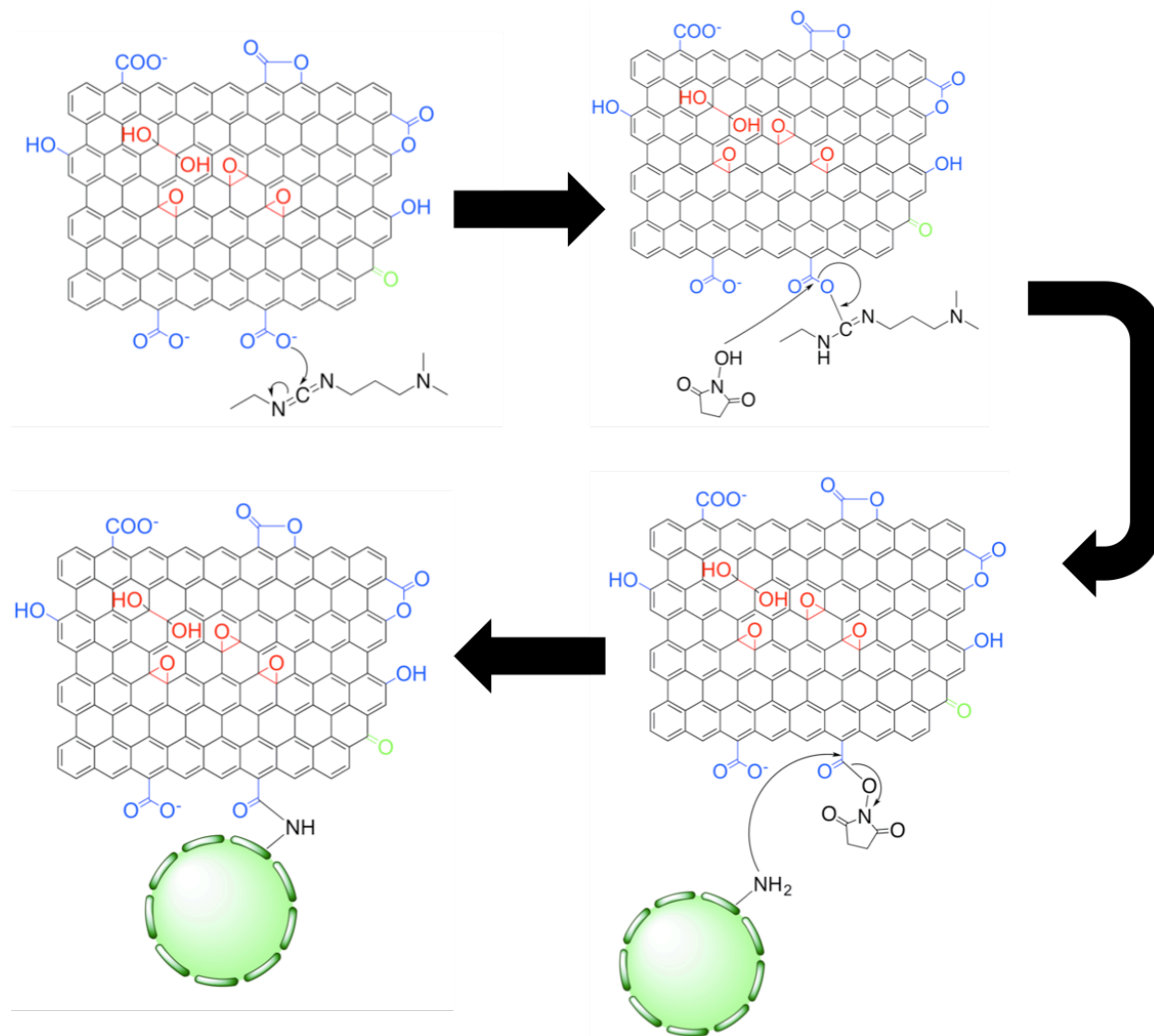
Figure 5: EDC/NHS GO – Fe NP crosslinking scheme

Figure 5. EDC/NHS crosslinking of GO and amine-functionalized Fe NPs.

Much like inorganic metal ions and nanoparticles, enzymes have been utilized to decompose carbon nanomaterials such as GO and carbon nanotubes.[24] Horseradish peroxidase

(HRP), an enzyme found in the roots of horseradish, can catalyze the degradation of these nanostructures due to the reaction between H_2O_2 and the enzyme's heme group (Figure 6a).[25] The heme-H_2O_2-substrate interaction acts as a three-step peroxidase cycle (Figure 6b). Fe^{III} is initially oxidized to form Compound I, which consists of an oxoferryl group ($Fe^{IV}=O$) and a porphyrin π-cation radical, while H_2O_2 is reduced to H_2O. Next, two single-electron transfers first generate Compound II, and then return the heme group to its native ferric state. These electron transfer steps are coupled with the oxidation of a substrate (AH). [26]
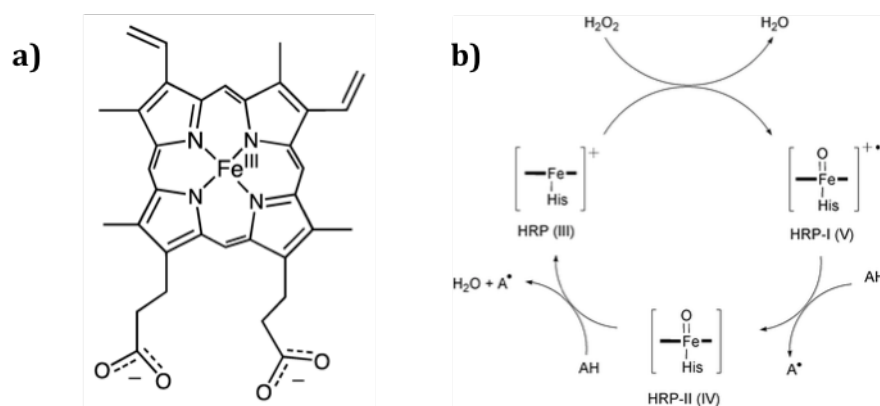
Figure 6: HRP heme and peroxidase cycle

Figure 6. HRP heme site structure (a) and catalytic peroxidase cycle (b); adapted from [25] (a) and [26] (b).

DNA origami, a unique approach to creating nanoscale architectures, exploits nucleotide base pairing in the design of a myriad of different shapes. The theoretical proposal for DNA as a basic nanoscale building block by Seeman[27] in 1982 and the demonstrated production of DNA origami by Rothemund[28] in 2006 has repeatedly shown the potential for use of this novel nanoscale architecture as a drug delivery agent.[29]

Yan and coworkers have shown that DNA-directed assemblies of anti-cancer drugs (such as doxorubicin) or enzymes (such as HRP) and DNA origami can be fabricated.[29, 30]

9

Furthermore, these enzymes can be discretely spaced onto the origami substrate. By combining the degradation capability of HRP and the spatial registration of enzyme-DNA origami architectures, well-defined patterning of carbon nanomaterials may be accomplished.

1.2   NANOCELLULOSE

While graphene and its derivatives have received an immense amount of attention, another carbon-based nanomaterial has increasingly piqued the interest of researchers. Nanocellulose (NC), a family of materials based on nanoscale architectures of cellulose, has a number of appealing attributes. The widespread availability of renewable NC sources, interesting mechanical properties, and potential for functionalization are all reasons why scientists from a wide range of fields are eager to develop NC technology. As such, novel applications for NC are being investigated with the hope that it could be used to improve or replace expensive and environmentally harmful materials.

The fundamental chemical structure of NC consists of stacks of cellulose chains,[31] as shown in Figure 7. Biosynthesis of NC results in the formation of alternating crystalline and amorphous areas, and these amorphous regions are preferentially cleaved during acid hydrolysis. The remaining nanoscale structures are known as nanocellulose crystals, and have varying dimensions based on the cellulose source and the acid hydrolysis conditions. For example, NC crystals obtained from sisal are 3-5 nm in width and 100-500 nm in length, while ramie has been used to produce NC crystals with widths of 5-10 nm and lengths of 50-250 nm. The abundant hydroxyl groups and large surface area provide functionalization sites for the modification of NC. Use of sulfuric acid for hydrolysis yields sulfate esters groups (Figure 7d). Carboxylation, esterification, silylation and acetylation have all been successfully used to modify NC.[32]
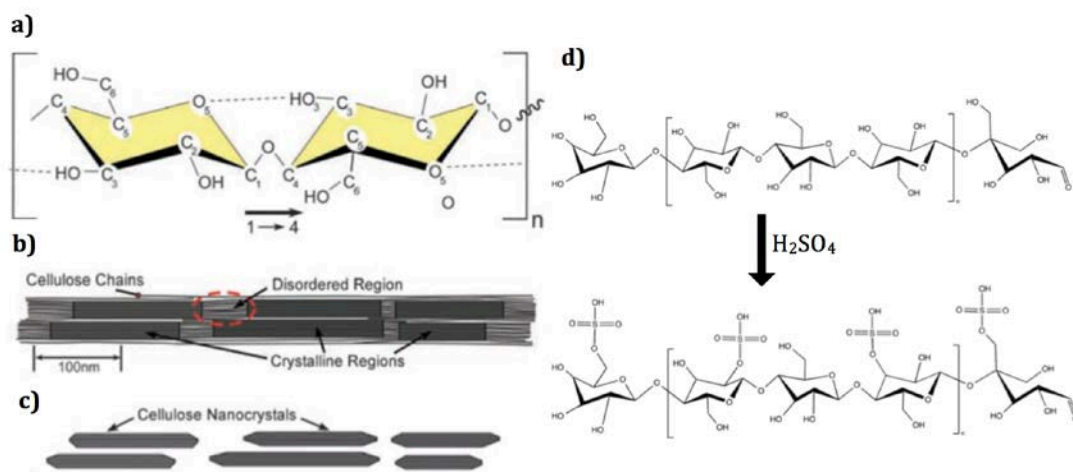
Figure 7: Cellulose molecular and nanoscale structure

Figure 7. Cellulose chemical structure of the monomeric unit (a), nanoscale architecture (b, c) and functionalization during hydrolysis in the presence of sulfuric acid (d); (a-c) adapted from [31].

Much like GO, NC has a huge potential impact in the invention and improvement of novel materials. NC, however, has not achieved the celebrity status that graphene-like materials have, and consequently have not been as thoroughly investigated in terms of toxicity. Preliminary reports have concluded that there is little or no evidence for the oral or dermal toxicity of NC, while pulmonary toxicity and cytotoxicity studies have yielded conflicting results.[33] As with any nanomaterial, even slight changes in particle dimensions, composition and functionalization can have a great impact on the interaction it has with a biological system. Since the NC source, production method and chemical treatments can all change these aforementioned qualities, it is imperative that the effect these attributes have on biotoxicity be assessed before implementation of NC.

Pulmonary exposure of NC crystals has been shown to produce a dose-dependent inflammatory response, oxidative stress and tissue damage in mice.[34] A similar effect is

generated from the inhalation of carbon nanotubes, although their interaction with human myeloperoxidase results in biodegradation of the nanomaterial.[35] Human myeloperoxidase (MPO), an enzyme most commonly expressed by neutrophils, is capable of generating hypohalous acids (such as HOCl) from H_2O_2 and the halide anion (*e.g.* Cl⁻). This reaction requires the heme cofactor, which acts much like it does in HRP by first forming Compound I. The acidic conditions of the neutrophil, however, allow for direct conversion from Compound I back to the native state by abstracting two electrons from the halide to form the hypohalous acid. Hypochlorite, with a redox potential of 1.48 V, is a stronger oxidant than any of the heme forms found in its catalytic cycle (Figure 8).[24] Therefore, there is a possibility that MPO could further oxidize and biodegrade NC, thus alleviating some concerns about the severity of any NC biotoxicity implications. The peroxidase cycle for MPO, with the potential hypochlorite pathway, is shown in Figure 8.
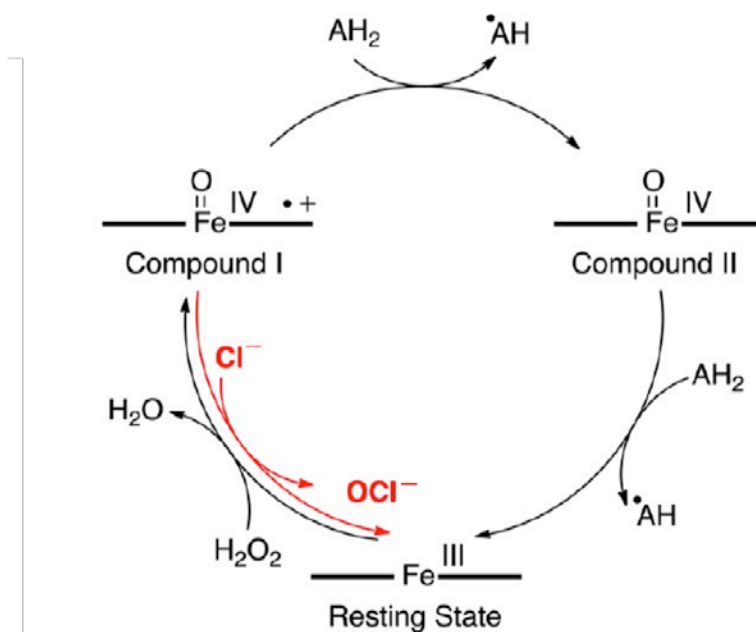
Figure 8: MPO peroxidase cycle

Figure 8. The peroxidase cycle for MPO; Adapted with permission from [24]. Copyright 2012 American Chemical Society.

13

1.3   CARBON NANOFIBER AND CHITIN

The immense research investigation into "traditional" carbon nanomaterials has spawned exploration into structurally and chemically related structures. The celebrity of carbon nanotubes has generated interest in a closely related architecture, vertically grown carbon nanofiber (VGCNF). Similarly, the increasing research and wide-scale availability of naturally occurring nanoscale structures such as nanocellulose has garnered attention to the applicability of chitin, another abundant nanocrystalline biopolymer. Since VGCNF and chitin are not as well-studied as their more illustrious counterparts, researchers must be careful to assess the toxicological risks of these structures individually, without making generalizations in regards to the safe application of these novel materials.

Carbon nanofibers share many of the same properties as their more well-known relative, carbon nanotubes (CNT). Both exhibit excellent thermal conductivity, electrical resistivity, tensile strength and tensile modulus.[36] CNTs, however, outperform VGCNFs in all of these aspects, albeit at a drastic increase in cost of production.[37] Differences in performance between VGCNF and CNT likely derive from differences in chemical architecture. CNTs are modeled as either single or multiple discrete layers of wrapped graphene sheets, with each sheet being a single continuous graphene plane. The architecture of VGCNFs, on the other hand, consists of a tube with graphite planes extending off of the hollow core either parallel or at an angle from the fiber axis. When growth occurs at an angle, a unique "stacked cup" or herring-bone structure is observed, similar to the nitrogen-doped carbon nanotube cups produced by Star and coworkers.[38] Graphitic growth, both angled and parallel to the fiber axis, creates defect sites in the tube, adversely affecting the aforementioned mechanical, electrical and thermal properties.

The production of VGCNF is accomplished using a chemical vapor deposition of a hydrocarbon in the presence of a metal catalyst. Commercially available Pyrograf® III nanofibers, manufactured by Applied Sciences Inc. (Ohio, USA), are produced using natural gas, iron pentacarbonyl (as a catalyst), ammonia and hydrogen sulfide (for catalyst dispersion and activation) feedstock gases in a gas phase reactor at 1100 °C.[39] Decomposition of iron pentacarbonyl provides iron nanoparticles that serve as catalytic growth sites. These catalysts then act as locations for the carbon feedstock gas to adsorb and decompose, dissolve through the catalyst, and finally form fiber-like growth on the catalyst surface opposite to adsorption.[40] Amorphous carbon coatings remaining on the fibers after the initial carbon vapor deposition growth are graphitized by annealing in vacuum or inert gas environments at 2000 – 3000 °C. This annealing post-treatment improves the physical characteristics of VGCNF, especially mechanical properties such as tensile strength and Young's modulus. The properties of VGCNFs, single-walled CNTs (SWNT) and multi-walled CNTs (MWNT) are compared in the following table.

Table 1. Comparison of VGCNF, SWNT and MWNT properties

Property	VGCNF	SWNT	MWNT
Diameter (nm)	50-200	0.6-1.8	5-50
Length (μm)	50-100	-	-
Aspect ratio	250-2000	100-10000	100-10000
Density (g/cm^3)	2	1.3	1.75
Thermal conductivity (W/m•K)	1950	3000-6000	3000-6000
Electrical resistivity (Ω cm)	1.00×10^{-4}	1×10^{-3} - 1×10^{-4}	2×10^{-3} - 1×10^{-4}
Tensile strength (GPa)	2.92	50-500	3.8
Tensile modulus (GPa)	240	1500	1000
Price ($/lb)	125	30,000 (90% pure)	350

Table 1: Morphological, thermal, electrical, and mechanical properties of VGCNF, SWNT, and MWNT (from [36]), and approximate manufacturing costs (from [37]).

Chitin is a biopolymer found repeatedly throughout nature, from arthropod shells and insect exoskeletons, to the cell walls of fungi. Its chemical structure is much like cellulose, with monomer units of N-acetylglucosamine connected using β-1,4 linkages. The hierarchical structure of the lobster (*Homarus americanus*) cuticle is presented in Figure 9.[41]
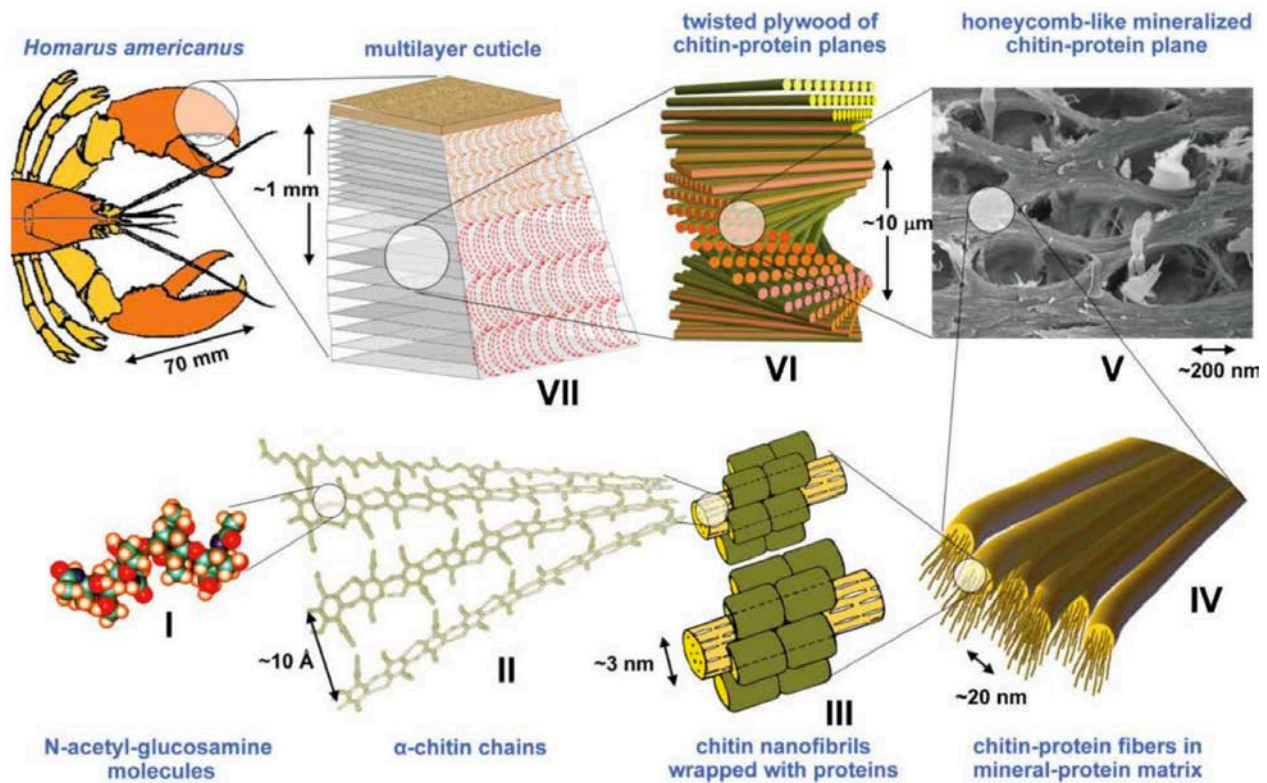
Figure 9: Hierarchical structure of lobster cuticle

Figure 9. Structural levels of the lobster cuticle. I) N-acetylglucosamine molecule; II) single chains of monomer units; III) chitin nanofibril bundles; IV) chitin bundle – protein matrix composite; V) SEM exhibiting honeycomb-like bundle – protein matrix; VI) twisting of individual chitin bundle planes; VII) millimeter-scale architecture. Adapted from [41].

In nature, chitin is most often utilized as a composite component. For example, calcium carbonate is combined with chitin in the shells of crustaceans, forming a tougher and more resilient material than pure chitin. The natural abundance and biodegradability make chitin an

appealing, readily available material with outstanding mechanical properties when used as a component in a nanocomposite. If an application could be found that utilized chitin, the 6 – 8 million tons of waste crab, shrimp and lobster shells produced annually might be effectively recycled and reused instead of simply discarded.[42]

The preparation of nanostructures of chitin (nanofibers and nanocrystals) is accomplished by first subjecting the chitin source (*e.g.* lobster, crab or shrimp shell) to an acid treatment, such as 2 M HCl, to remove calcium carbonate matrix. Proteins that surround the individual chitin nanostructure to form nanobundles are removed using a concentrated base (for example 2 M NaOH) at reflux. Depigmentation can be achieved by subjecting the samples to refluxing ethanol. Finally, a mechanical grinding of the purified chitin is then used to obtain the final nanostructured chitin.[43]

Although VGCNF and chitin offer appealing attributes and potential applications, especially as mechanical fillers due to their individual or composite mechanical strength, the toxicity of these materials must be assessed before their implementation in consumer products can be realized. Since VGCNFs shares many similarities with CNTs, the asbestos-like effect observed for CNTs may also hold true for VGCNFs. The health risks of nanoscale forms of chitin, much like NC, are not well established. Even though the interaction between the human body and chitin has been thoroughly investigated, new potential interactions may arise for chitin architectures that have dimensions comparable to respiratory bronchioles in the human lung, thus posing a new and unique health risk. Enhanced understanding of the relationship between morphology, chemistry, and biological interaction between VGCNF, chitin, and the human body must be comprehensively analyzed so that the safe usage of these exciting new materials can be achieved.

1.4   CHARACTERIZATION TECHNIQUES

Nanomaterials have long been characterized using a number of microscopy and spectroscopy techniques to assess morphological features. The nanoscale dimensions of materials such as GO and NC make them well-suited for electron microscopy analysis methods like transmission electron microscopy (TEM) and scanning electron microscopy (SEM), in addition to scanning probe systems such as atomic force microscopy (AFM). The negative surface charges of GO and NC (when prepared using acid hydrolysis) also allow for the aqueous colloidal stability necessary to perform dynamic light scattering (DLS) investigations. Use of these methods is a straight-forward approach in the evaluation of nanomaterial degradation, and their implementation is aided by understanding of the underlying physical processes involved. Examples of their prior use in similar schemes also provides valuable information in regards to expected results, resolution limits, and implementation.

Electron microscopy methods, such as TEM and SEM, are commonly employed to image carbon nanomaterials like GO and NC, albeit by operating under fundamentally different approaches. For both techniques, use of electrons as the probe allows for the resolution of much smaller features than optical microscopy, as the de Broglie wavelength for the electron under the imaging conditions is much smaller than the wavelength of visible light. TEM relies on the scattering of an electron beam by the sample to reveal information about the morphology, crystallinity, and composition of the sample. These qualities all affect the scattering behavior of the incident electron, such as the probability of it occurring and the angle at which the electron is deflected. Sample areas that are composed of either denser material or higher atomic number elements will scatter electrons with a higher probability and at higher angles due to the interaction between the electron and the sample nuclei. Electrons that are either not scattered or

scattered at small angles are "transmitted" through the sample, and their spatial detection used to create an image. Stains, which are composed of high atomic number elements such as uranium, are often employed for biological samples (including NC), as the low atomic mass elements (such as C, H, and O) combined with the low density of material create relatively few scattering events by themselves. Negative stains provide a dark background for the sample, and improve the resolution due to an increase in contrast.

The collection of secondary and backscattered electrons is used by SEM in the imaging of a material. Secondary electrons arise as the product of interaction between the incident electron beam and the sample, whereby the incident beam collides with and ejects the secondary electron from the sample. The release of the secondary electron and subsequent relaxation of an outer shell electron produces an X-ray photon, whose energy is specific to an element and can be further used to assess the chemical composition of the sample *via* energy-dispersive X-ray spectroscopy (EDX). The detection of backscattered electrons, which relies on high angle scattering of incident electrons off of the sample nuclei, is especially useful for providing compositional contrast. As higher atomic number elements have a higher probability for producing backscattered electrons, the intensity of detected backscattered electrons can be correlated with different element types for a sample with a known composition. The ability to image the morphology and chemical makeup of a sample concurrently makes SEM a powerful tool for the evaluation of nanomaterials.

Scanning probe microscopy techniques utilize interactions between a needle-like probe or "tip" and the sample to image the sample surface. AFM, a type of SPM, works by moving the tip across the sample while at very small distances (typically less than 10 nm) to create a raster. When the tip comes close enough to the surface, van der Waals forces cause a deflection of the

cantilever holding the tip, and this deflection is detected through the change in reflection of a laser off the back of the cantilever and onto a photodiode detector. Commonly, AFM functions in tapping mode, whereby the tip is oscillated at a set frequency and a piezoelectric servo functions to maintain the amplitude of oscillation of the tip while recording the change in tip height as the measured sample height. This approach mitigates damage to the tip or sample, allowing for repeated scanning of the same sample areas. The lateral resolution of images generated using AFM is limited by the sharpness of the tip used, which is typically less than 10 nm, making AFM functional for the measurement of nanoscale dimensions.

Information on the size of nanoparticles in solution is possible using DLS, which gives measurements such as hydrodynamic radius of the material as well as their dispersity. This method works by first measuring the intensity of scattered light at a number of time points following the initial illumination. These intensity measurements as a function of time are used to create a correlation function, which is related to the particle size. For a smaller particle, the exponential decay of the correlation function is faster due to a higher diffusion rate, which is a consequence of Brownian motion. Reliance on Brownian motion dictates that no other particle movements are occurring contemporarily, such as sedimentation, and therefore the particle must form a stable colloidal solution. The reported size for a DLS measurement is the hydrodynamic radius, which consists of the particle as well as any ions or solvent that move with it as it diffuses through the solution. Figures 10, 11, and 12, summarizes the physical processes for these four characterization techniques, and show representative examples from literature.
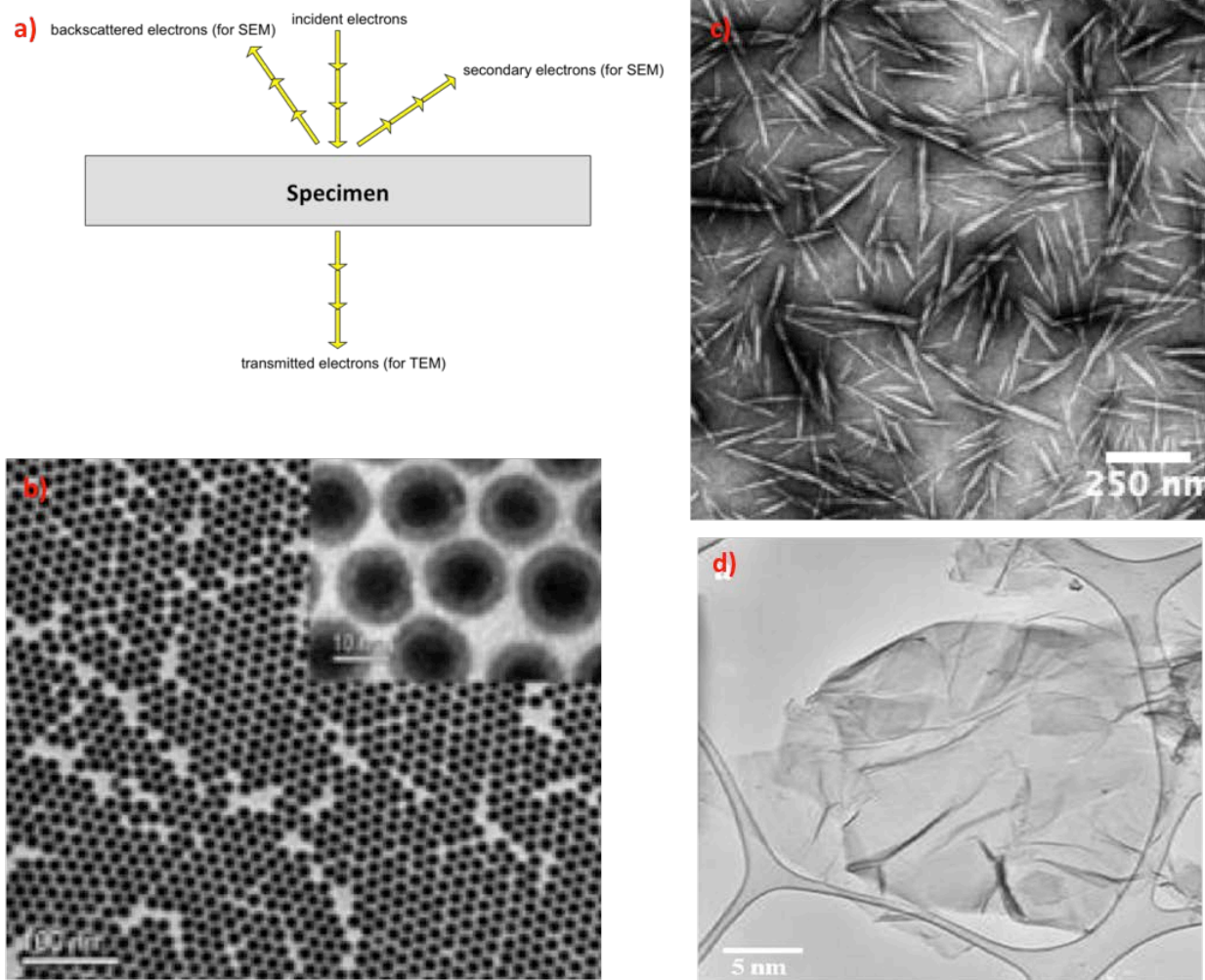
Figure 10: Electron microscopy - electron detection and TEM examples

Figure 10. Details for techniques used in electron microscopy nanomaterial characterization and representative TEM micrographs. a) Electron scattering angles and detection in TEM and SEM; b) Fe NP, adapted with permission from [44]. Copyright 2006 American Chemical Society; c) NC from ramie, adapted with permission from [32]. Copyright 2010 American Chemical Society. d) GO, from adapted from [45].
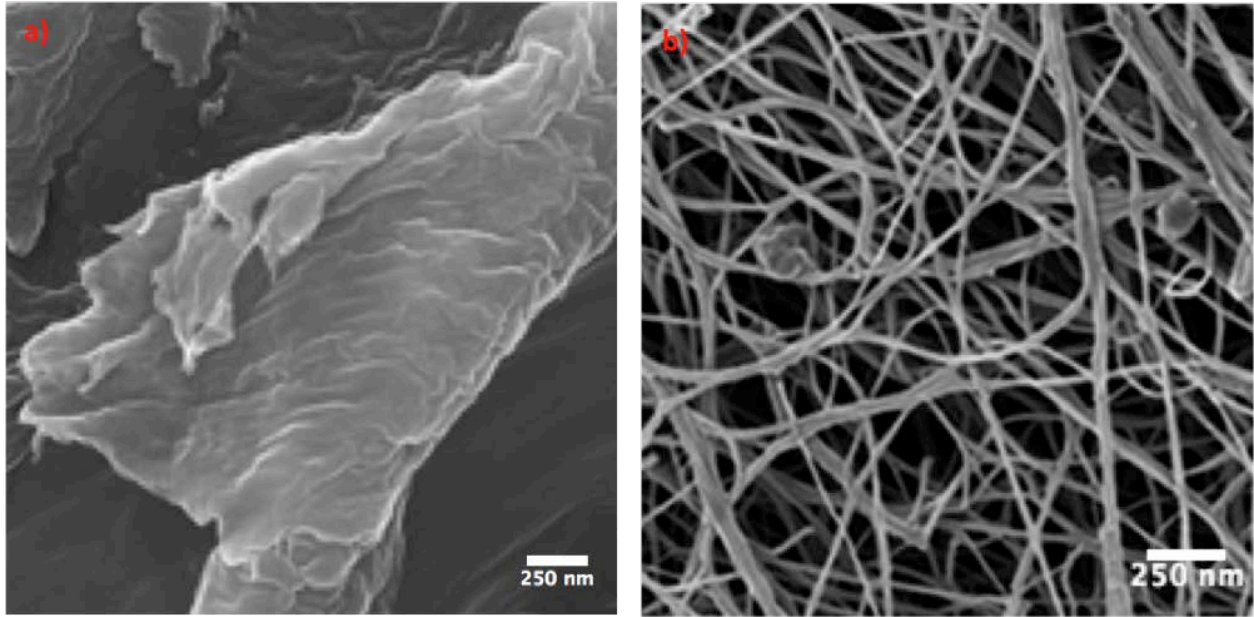
Figure 11: Scanning electron microscopy and examples

Figure 11. Representative SEM micrographs. a) GO, adapted from [46]; b) bacterial nanocellulose sputtered with Au, adapted from [47].
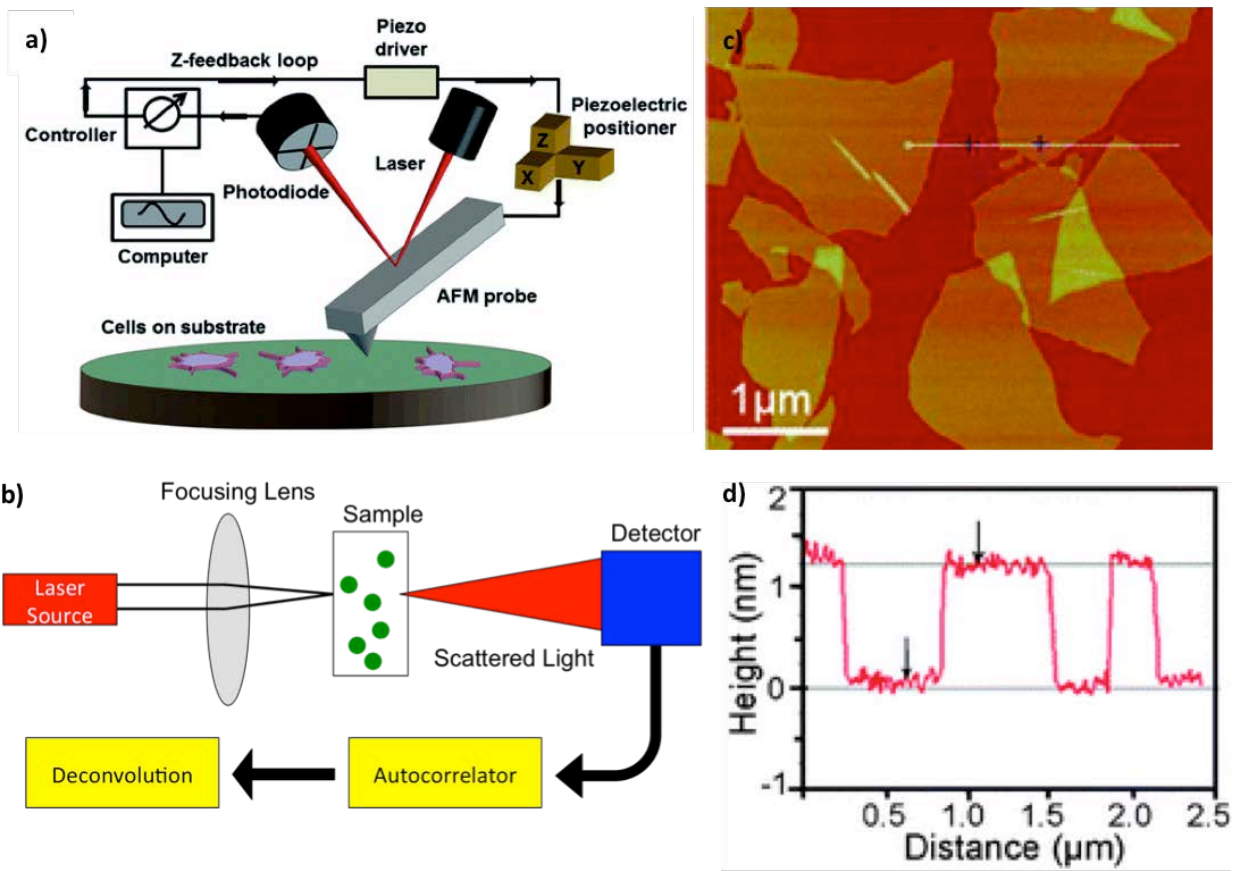
Figure 12: Atomic force microscopy and DLS instrumentation and example

Figure 12. AFM and DLS instrumentation details and representative AFM micrograph. a) AFM tip instrumental design, adapted from [48]; b) DLS instrumentation design; c) AFM image of GO, adapted from [49]; d) height analysis of line drawn in (c), adapted from [49].

2.0   RESEARCH RESULTS

To address the stability of carbon nanomaterials such as GO and NC, a number of experiments have been performed where these materials were subjected to a variety of environmental conditions and the degradation characterized. First, GO decorated with iron nanoparticles was subjected to a photo-Fenton environment in an attempt to localize and control the registration of degradation sites (*i.e.* holes). Next, the oxidation of NC through MPO catalysis was investigated to predict the ability of the enzymatic environment to degrade or convert NC into a form that does not elicit an inflammatory pulmonary response. Similarly, the enzymatic degradation of GO was explored using a novel DNA-HRP origami structure as a proof-of-concept that DNA origami can be utilized as a template for the patterned degradation of the GO sheet. Finally, the nanoscale morphology of VGCNF and chitin were established. Characterization was accomplished using electron (TEM, SEM) and scanning probe (AFM) microscopies, as well as with dynamic light scattering (DLS).

24

2.1   DEGRADATION OF GRAPHENE OXIDE

2.1.1   Methods and Materials

Transmission Electron Microscopy (TEM). TEM imaging was performed using an FEI Morgagni microscope operating at 80 keV. Samples were prepared by drying 3 µL of sample solution on a TEM grid (Electron Microscopy Sciences, Hatfield, PA) made of carbon film on a copper support (400 mesh).

Atomic Force Microscopy (AFM). AFM imaging was performed using a Multimode scanning probe microscope (Veeco) in tapping mode. Freshly-cleaved mica was used as sample surface for all samples. For samples with GO, the freshly-cleaved mica surface was functionalized with APTES by incubating the surface with 50 µL of 0.05% APTES aqueous solution for 1 min, followed by rinsing with Nanopure H_2O and drying with N_2 gas. The sample solution (5 µL) was then incubated on the surface for 2 min. After lightly dipping the mica in DI water, the mica was carefully dried with N_2 gas. An ACL probe (AppNano, Santa Clara, CA) was utilized at a frequency between 160-225 kHz, an amplitude set point between 1.5-1.8 V, and a minimized drive amplitude, generally between 100-300 mV. The resulting images were processed using Gwyddion software.

Reagents and Materials. All reagents were used as received without further purification. Graphene oxide in aqueous solution (5 mg/mL) was purchased from Graphene Supermarket. Hydrogen peroxide (30%), concentrated hydrochloric acid, iron chloride hexahydrate, (1-Ethyl-3-(3-dimethylaminopropyl)-carbodiimide)   (EDC),   N-hydroxysuccinimide   (NHS)   and (3-aminopropyl)triethoxysilane (APTES) was purchased from Sigma-Aldrich (St. Louis, MO). Sodium acetate (NaAc, anhydrous) was purchased from JT Baker (Center Valley, PA).

Poly(vinylpyrrolidone) (PVP, average molecular weight of 40,000 Da) was purchased from OmniPur (Billerica, MA). Amine-functionalized iron oxide (Fe_3O_4) nanoparticles were purchased from Ocean NanoTech. Nanopure water (18.2 MΩ resistivity) was used unless noted otherwise.

2.1.2   Iron Oxide Nanoparticle Synthesis

Polyhedral PVP-capped Fe NPs. Polyhedron-shaped α-Fe_2O_3 NPs were produced using a hydrothermal synthesis protocol by Zhu *et al*.[50] In short, 4 mM FeCl$_3$•6H$_2$O, 40 mM NaAc and 0.3309 g PVP were mixed in 10 mL H$_2$O and stirred at 40 °C for 2 h. The solution was then transferred to an autoclave and heated at 200 °C for 18 h in an oven. After allowing the autoclave to cool (1 h), the precipitate was collected using centrifugation (10,000 rpm for 45 min), then the pellet was retrieved *via* vacuum filtration. After drying the filter paper with the retentate at 70 °C for 18 h, the Fe NPs were collected by sonicating the filter paper in ethanol.

Acicular Fe NPs. Acicular α-Fe_2O_3 NPs were produced using a protocol by Suber *et al*.[51] A solution of 2×10^{-2} M FeCl$_3$•6H$_2$O and 3.8×10^{-4} M NaH$_2$PO$_4$ was boiled in H$_2$O for 3 days. The reaction precipitate was then collected using centrifugation (10,000 rpm for 30 min), and the pellet retrieved and washed with H$_2$O *via* vacuum filtration. After drying the filter paper with the retentate at 75 °C overnight in an oven, the Fe NPs were collected by sonicating the filter paper in ethanol.

2.1.3 Covalent Attachment of Iron Oxide Nanoparticle to Graphene Oxide

The decoration and attachment of GO with Fe NPs was accomplished through the use of EDC/NHS coupling between amine-functionalized Fe NPs and the carboxylic acid groups on GO. First, EDC/NHS functionalized GO was prepared by mixing 1.28 mg EDC, 1.11 mg NHS and 5 mL GO (560 mg/L, aqueous) and stirred overnight. This solution was then dialyzed overnight (3.5-5 kD Float-a-Lyzer membrane). The attachment of Fe NPs was then performed by mixing 179 µL of EDC/NHS functionalized GO, 20 µL amine-functionalized Fe NP (50 mg/L, in 10 mM PBS) and 801 µL PBS buffer (10 mM). This solution was incubated on a hot plate at 80 °C for 2 h, briefly shaking every 30 min to redisperse the materials. The EDC/NHS-GO/FeNP solution was then dialyzed overnight.

2.1.4 Photo-Fenton Reaction Experiment Design

The degradation of GO under photo-Fenton reaction conditions in the presence of Fe NPs was conducted by first mixing GO and polyhedral Fe NP reagents in H_2O and sonicating the mixture for 15 min to promote separation of GO sheets and decorate them with Fe NPs. Following sonication, the pH of the reaction solution was lowered to 2-3 by the addition of diluted HCl. The photo-Fenton reaction was initiated by the addition of 18.75 mM H_2O_2 and by placing the reaction vessel approximately 6 cm from the UV source, a Blak-Ray B100AP, 100 W long wave UV lamp (Upland, CA). A quartz cuvette with a 1 cm path length (World Precision Instruments; Sarasota, FL) was utilized as the reaction vessel. The cuvette was partly submerged in flowing tap water to maintain a constant reaction solution temperature of 22 °C and inhibit solvent evaporation.

Investigation of the response of EDC/NHS-GO/FeNP under photo-Fenton conditions was performed using a partially different experimental setup. In a quartz cuvette, 2 mL H_2O and 0.5 µL concentrated H_2SO_4 were mixed, making the pH of the solution 2-3. Then, 1 µL of 30% H_2O_2 was added. Peroxide test strips revealed the peroxide concentration to be between 30-100 mg/L. Next, 200 µL of EDC/NHS-GO/FeNP was added to the solution. Finally, the solution was illuminated with 254 nm UV light from an Entela Mineralight lamp (115 V, 0.115 Amp) for the denoted duration of time.

2.1.5   Iron Oxide Nanoparticle Characterization

To ensure the quality of the synthesized and received Fe NPs, microscopy techniques were employed and compared to published results. These characterizations are summarized in Figures 13 and 14. Images collected using TEM show that the syntheses were indeed successful in reproducing the original results, as the shape and size of the polyhedral and acicular Fe NPs match well the expected outcomes. Figure 13 compares the expected (literature-reported) results with the polyhedral Fe NPs that were synthesized in-house. While the published nanoparticles displayed a more uniform morphology and homogeneity, polyhedral Fe NPs with acceptable shapes and sizes were able to be produced. Well-defined acicular Fe NPs with a highly uniform shape and size were also effectively produced based on the published protocol, as shown in Figure 14. The highly unique shape of these Fe NPs were chosen such that the localized degradation of GO would resemble the shape of the nanoparticle.
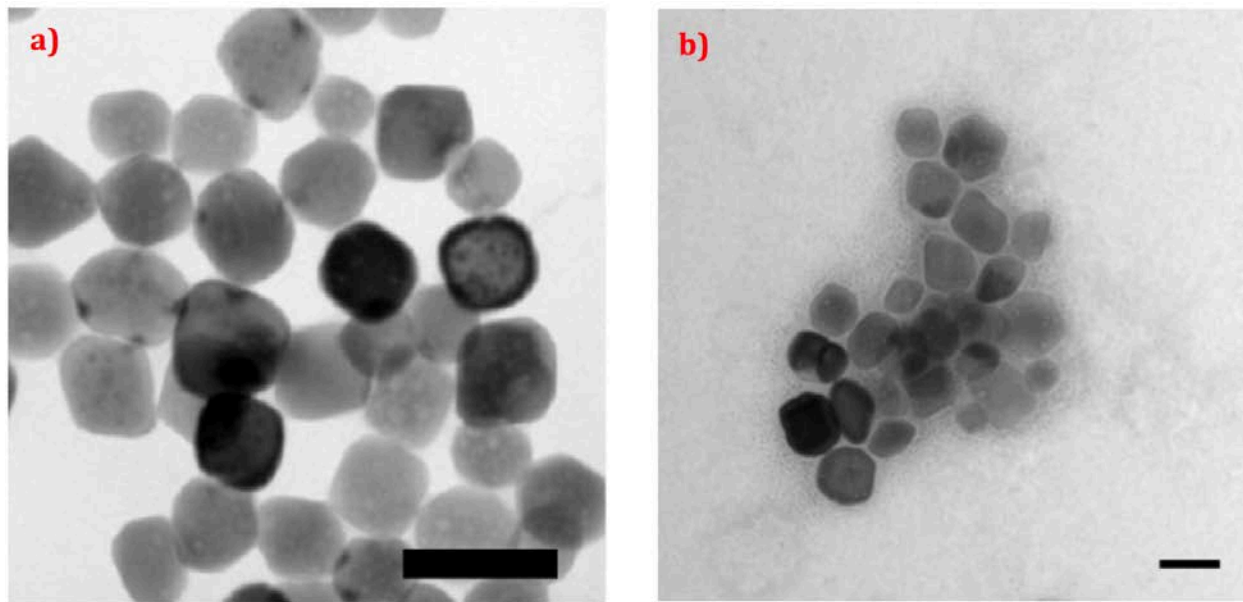
Figure 13: Polyhedral Fe NP TEM micrographs

Figure 13. TEM characterization of polyhedral Fe NPs. a) TEM image taken from protocol reference publication; adapted with permission from [50]. Copyright 2012 American Chemical Society. b) Typical TEM image of as-synthesized Fe NPs, showing similar scale and morphology to reference image. Scale bar 100 nm for both images.
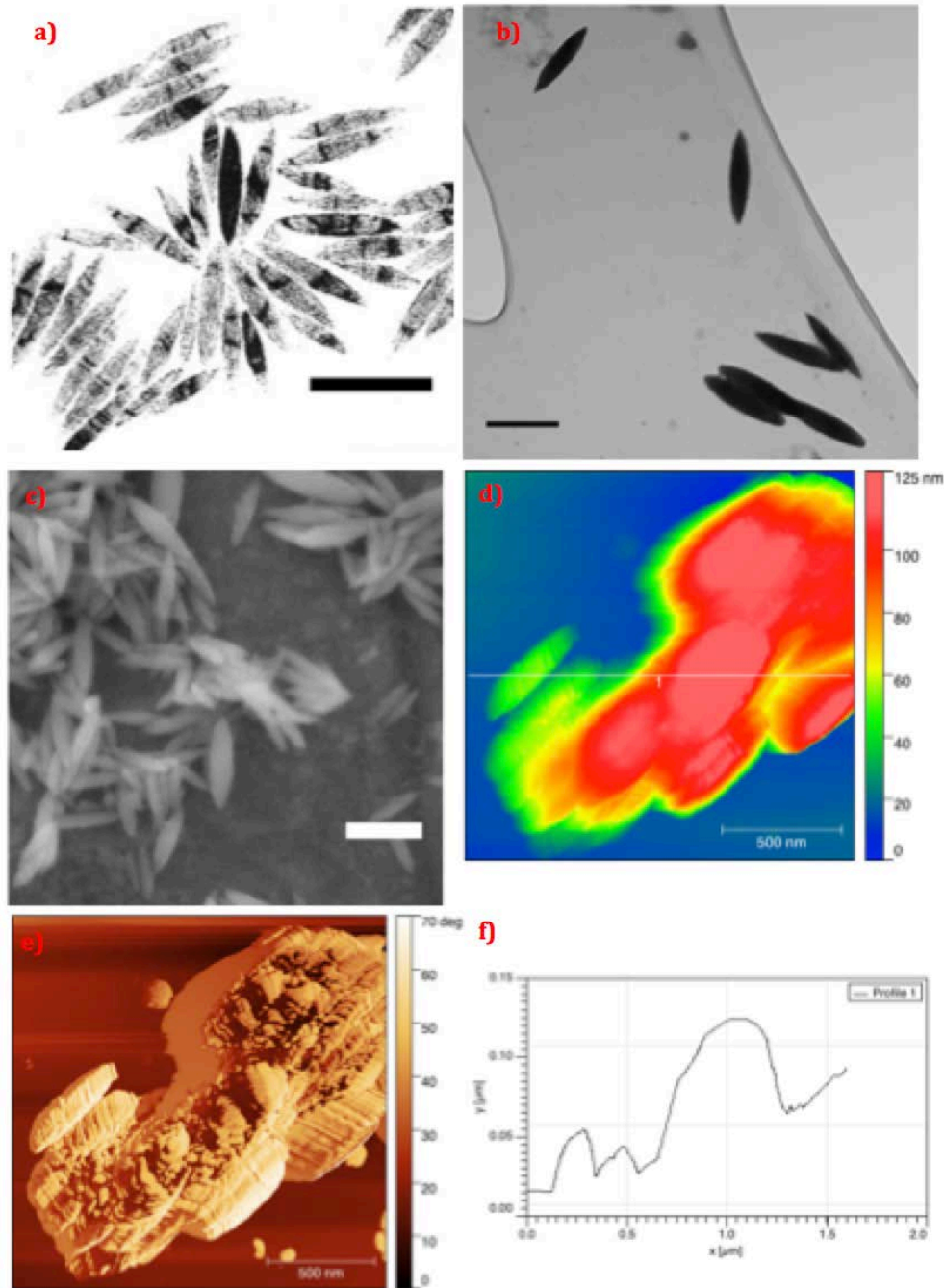
Figure 14: Acicular Fe NP - microscopy characterizations

Figure 14. Microscopy characterization of acicular Fe NPs. a) TEM image taken from reference protocol publication; adapted from reference [51]; b) TEM, c) SEM, d) AFM height, and e) AFM phase images of as-synthesized acicular Fe NPs; f) height profile of line drawn in (d). Scale bar 500 nm for all images.

The characterization results for both types of Fe NPs reveals the aggregation behavior seen with α-Fe$_2$O$_3$ nanoparticles due to their nano-sized features and ferromagnetic properties. However, the positive surface charge for Fe NPs in acidic solution can be used to help disperse them onto GO sheets, which are negatively charged due to the low acidity constant for carboxylic groups (pK$_a$ = 4.3).[52] While both types of Fe NPs do not form colloidal solutions with long-term homogeneous dispersions, the presence of the PVP capping agent on the polyhedral Fe NPs did improve their colloidal stability. For this reason, the Fe NP-GO reaction mixtures utilized the polyhedral Fe NPs for degradation studies.

2.1.6   EDC/NHS - GO/Fe NP Characterization

Observation of the amine-functionalized Fe NPs using TEM (Figure 15a) showed the nanoparticles had the expected size, roughly 20 nm. They were thus used as received. Following the EDC/NHS treatment of GO, TEM and AFM analysis to assess any morphological changes that may have resulted. Representative micrographs are presented in Figure 15b-d. Assessment of the EDC/NHS-GO/FeNP material after linking the two substituents was also made using TEM, and these results are shown in Figure 15f.

31
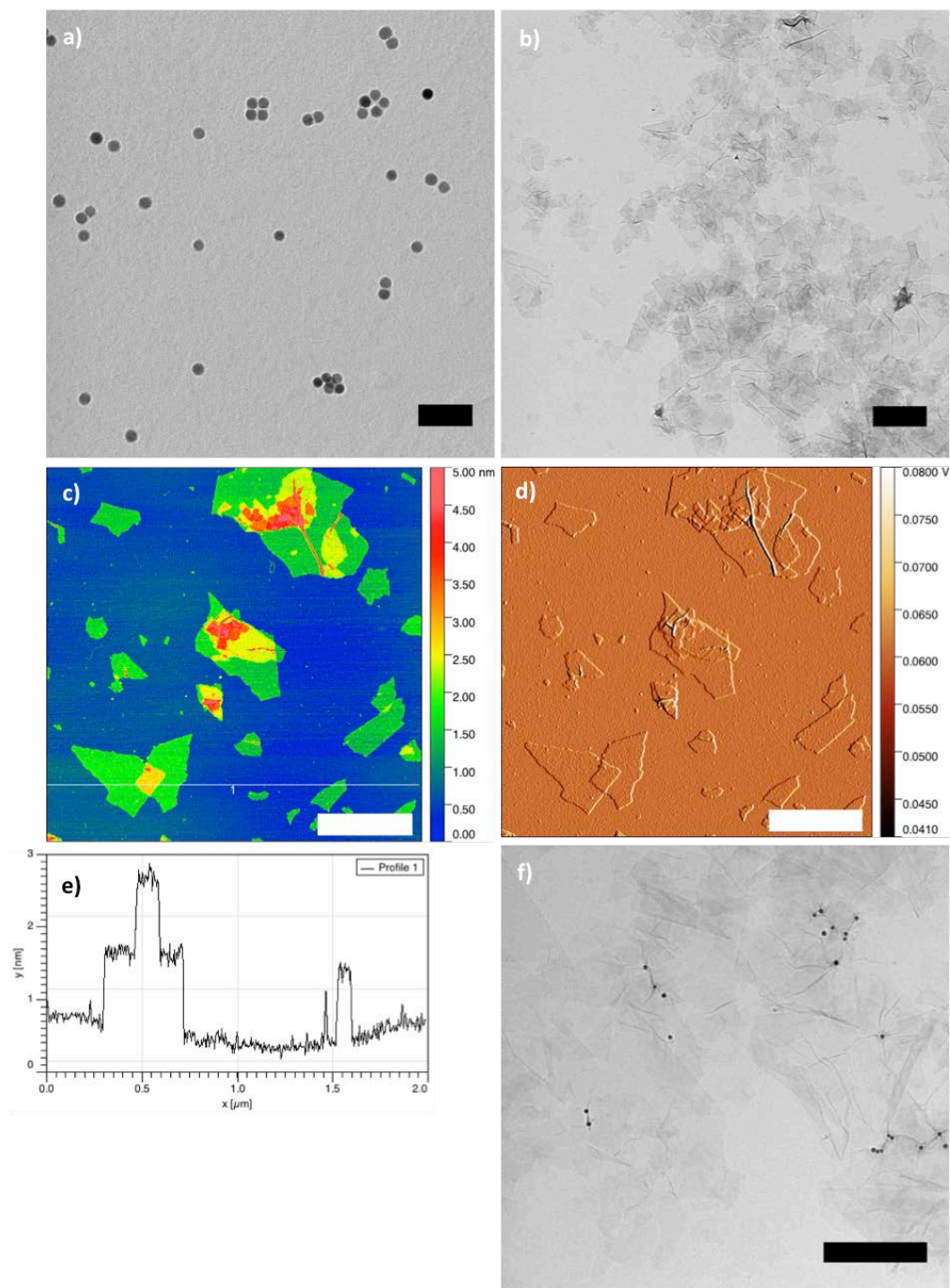
Figure 15: EDC/NHS – GO/Fe NP materials microscopy characterization

Figure 15. EDC/NHS – GO/Fe NP coupling materials. a) amine-functionalized Fe NPs TEM. EDC/NHS treated GO b) TEM, c) height AFM, and d) amplitude AFM. Profile for line drawn in (c) shown in (e). f) EDC/NHS – GO/FeNP product TEM image. Scale bars: a) 100 nm; b) 800 nm; c, d) 500 nm; f) 200 nm.

32

2.1.7 Photo-Fenton Reaction Results

The exposure of GO to photo-Fenton conditions in the presence of Fe NPs was effective in the formation of localized degradation sites. As shown in Figure 16, distinct holes can be seen in the GO sheet both in the area of the Fe NP and in places well-removed from nanoparticle. Since the reaction is performed in solution, the Fe NP may move away from the temporary adsorption point on the GO sheet once the degradation has occurred and re-adsorb in another area. GO sheets do not show any sign of degradation (hole formation) prior to the exposure of photo-Fenton reagents. Similar results were observed for both the GO – polyhedral FeNP and EDC/NHS – GO/FeNP reaction mixtures.

Imaging with AFM of the material after exposure to the photo-Fenton reaction conditions shows that degradation occurs preferentially at edge sites. As shown in Figure 17, sheets are formed with rounded and jagged edges that appear markedly different than the pseudo-straight edged material that dominates before the reaction occurs. The hydroxyl attack and subsequent oxidation of GO would most likely occur at reactive sites on the sheet. Since GO is thought to be well-decorated with alcohol, carboxylic acid, and lactone functionalities on the sheet edges, the degradation of GO will most likely proceed from the outside in. Hole formation on the basal plane of the sheet is also possible *via* reaction between hydroxyl radical reactions with interior olefin and epoxide functionalities, as well as with any oxygen-containing moieties that decorate the edges of pre-existing defect sites. Incubation of the EDC/NHS – GO/FeNP material in a control experiment that omitted H_2O_2 did not show any evidence of hole formation or edge degradation, as shown in Figure 18.
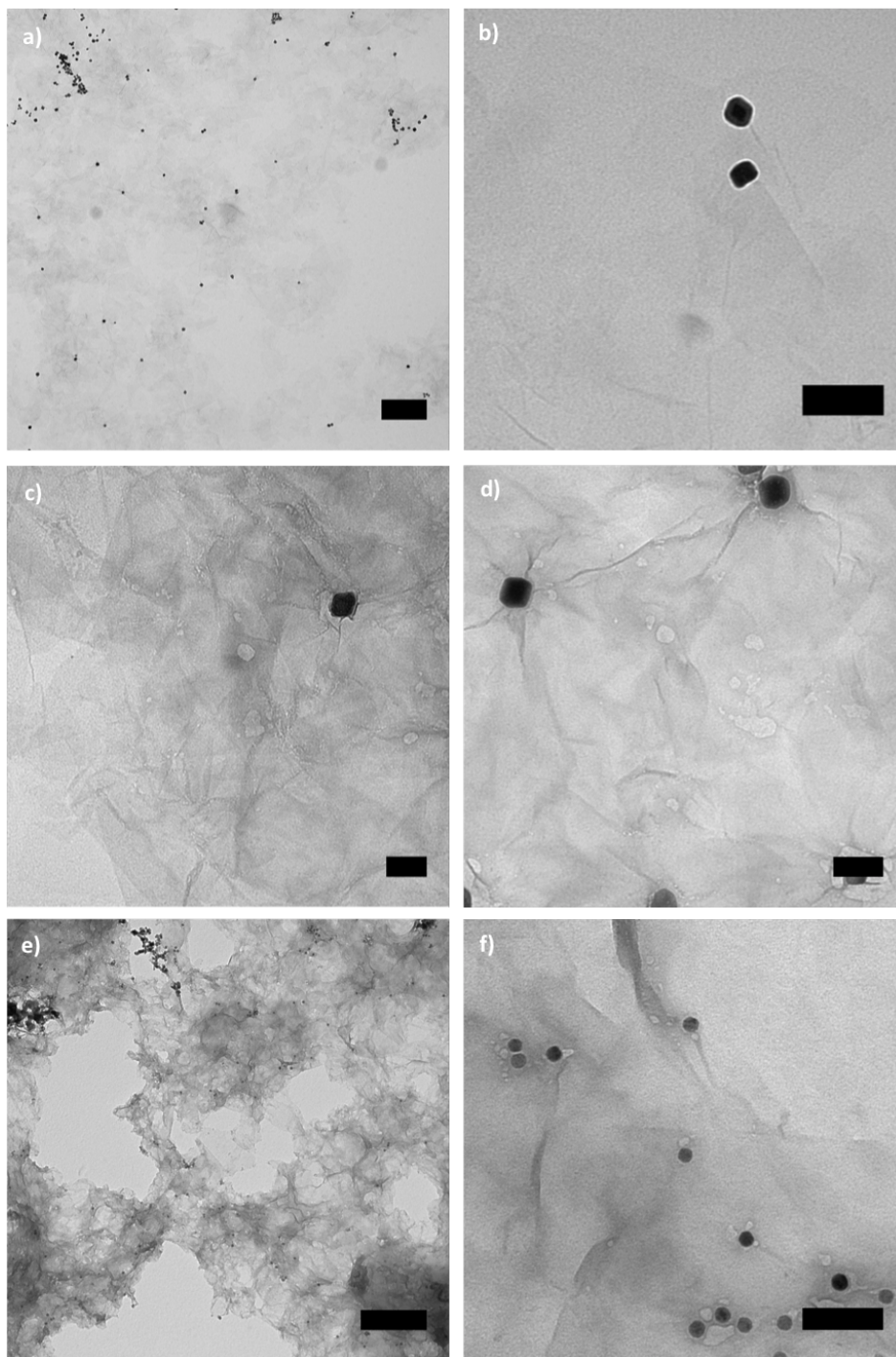
Figure 16: GO – Fe NP - photo-Fenton reaction TEM results

Figure 16. GO – polyhedral Fe NP reaction mixtures in H$_2$O (a, b) and after 2 h under photo-Fenton reaction conditions (c, d). EDC/NHS – GO/Fe NP reaction mixtures after 12 h under photo-Fenton reaction conditions (e, f). Scale bars: a) 1 µm; b-d) 100 nm; e) 500 nm; f) 100 nm.
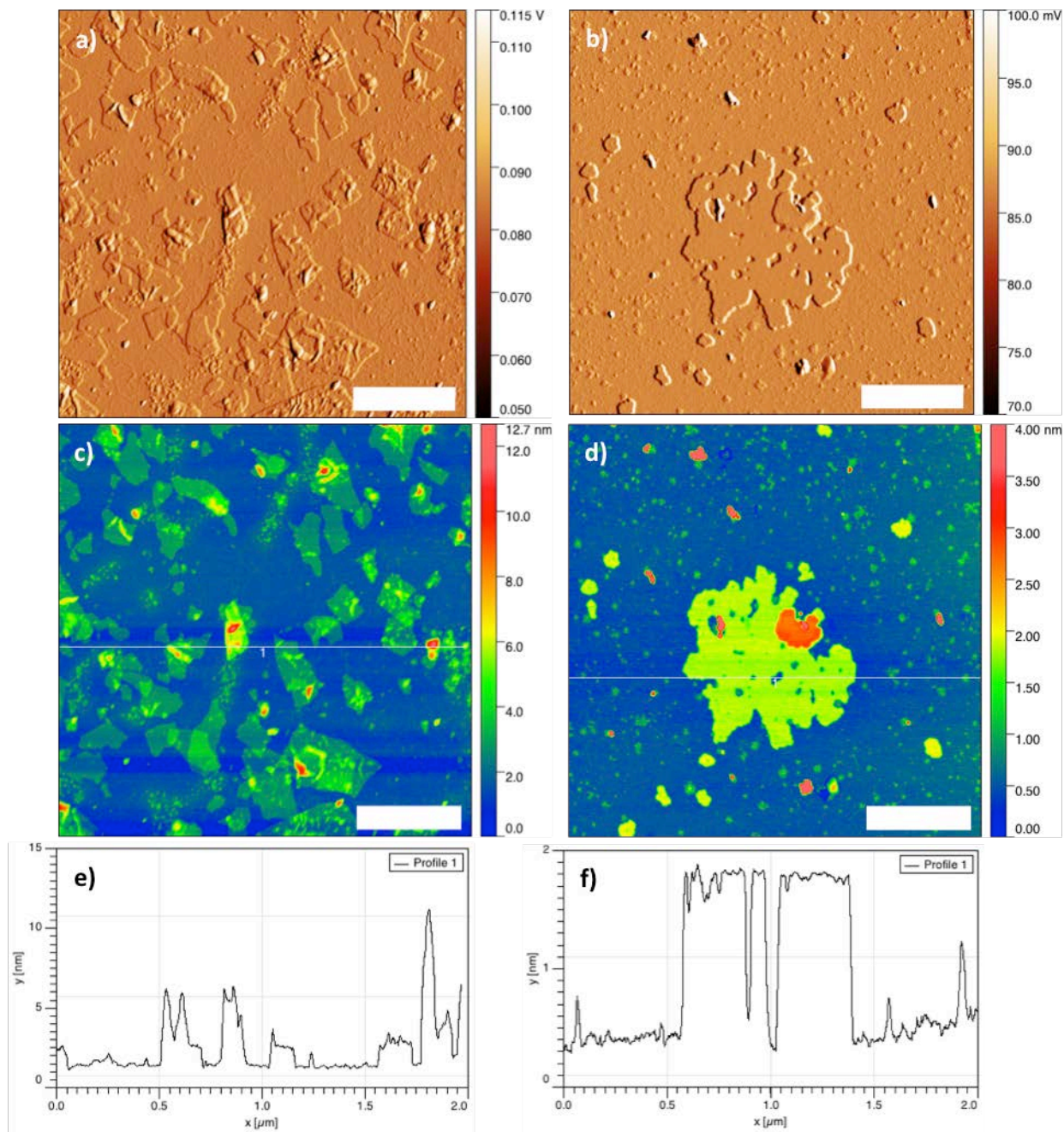
Figure 17: EDC/NHS – GO/FeNP photo-Fenton reaction results - AFM imaging

Figure 17. AFM characterization of EDC/NHS – GO/FeNP before (a, c, e) and after (b, d, f) 12 h of photo-Fenton reaction conditions. Amplitude AFM (a, b), height AFM (c, d), and profile lines drawn in (c, d) given in (e, f, respectively) shown. Scale bars 500 nm for all images.
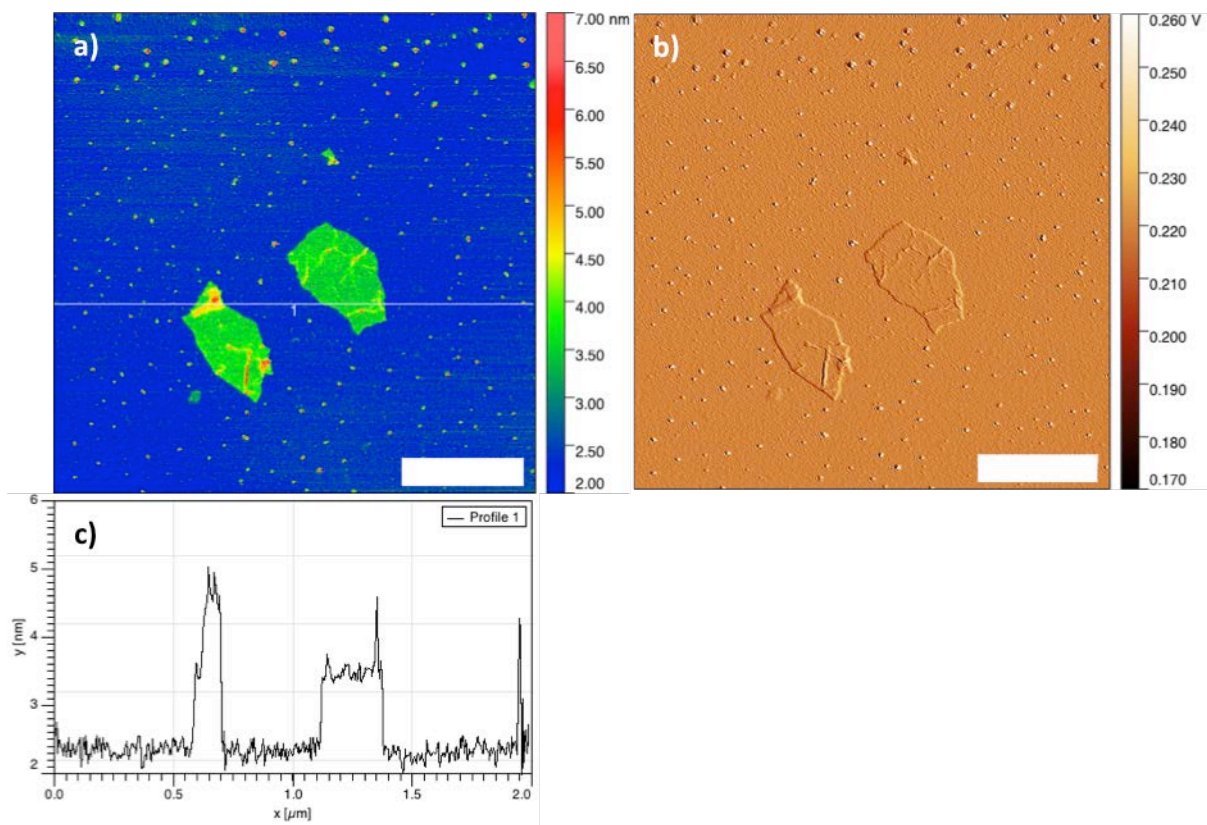
Figure 18: EDC/NHS – GO/FeNP control reaction results - AFM imaging

Figure 18. AFM characterization of EDC/NHS – GO/FeNP after 6 h of photo-Fenton reaction conditions, minus H_2O_2. Height AFM (a), amplitude AFM (b), and profile for line drawn in (a) given in (c) shown. Scale bars 500 nm for all images.

2.1.8   Discussion

Characterization of the interaction between GO and Fe NPs under photo-Fenton reaction conditions using TEM was successful in showing a change in morphology for GO. The most apparent change was the evolution of holes in the GO basal plane upon irradiation. Based on these results, it can be concluded that the Fe NP is capable of creating degradation-causing

species, likely hydroxyl radicals. Furthermore, the GO sheets are susceptible to degradation by Fe NPs when H_2O_2 is present in an acidic environment.

The TEM micrographs reveal that hole formation occurred at distances further from the observed Fe NP than predicted. This could be due to the fact that the polyhedral Fe NPs were not covalently attached or anchored to a consistent location on the GO sheet, but were merely attracted to the GO based on Coulombic forces. It is possible that multiple GO-Fe NP attachment/detachment events occurred over the course of the reaction, whereby the Fe NP diffuses to another spot on the same sheet or a different sheet. Each event allowed for hole formation at a different location, creating GO decorated with holes in many areas as opposed to just those areas local to the Fe NP. Another possibility is that the reaction solution was not actually at room temperature. Since the equations used to predict the 3-D diffusivity of the hydroxyl radical were functions that are linearly correlated with temperature, any increase in temperature will result in an increase in diffusivity. It was attempted to maintain the temperature of the reaction solution by keeping the reaction vessel partially submerged in circulating water, yet it is still possible that local increases in temperature resulted from the exposure of the solution to the heated UV lamp. Investigation using EDC/NHS – GO/FeNP showed hole formation more localized to the Fe NP site. However, since the reaction is performed in solution, it is possible that noncovalent interactions between GO and Fe NPs allowed for hole formation away from observed Fe NPs due to diffusion of the sheets.

Control experiments which omitted the addition of H_2O_2 exhibited no evidence of degradation using AFM analysis, as shown in Figure 18. Comparison of the images produced of the material before and after the reaction using only an acidic environment and UV light exposure reveal wrinkled sheets with a sheet thickness of approximately 1 nm. Based on these

results, it can be concluded that H_2O_2 is necessary for the degradation of GO to occur in the presence of iron oxide nanoparticles.

2.1.9 Conclusion

The degradation of GO under photo-Fenton reaction conditions catalyzed by Fe NPs is capable of producing a unique holey 2-D carbon nanostructure. This facile treatment of readily available and easily produced materials provides a straight-forward approach to create well-defined holes in the basal plane of GO. Whereas photo-Fenton treatment of GO using iron ions has been shown to induce the formation of many small holes,[16] it may be desirable for some applications to keep the majority of the GO plane intact and only create some distinct holes. Furthermore, the registry of these holes may be better controlled through the anchoring of Fe NPs to distinct locations on the GO sheet *via* covalent bonding.

2.2   NANOCELLULOSE: CHARACTERIZATION AND DEGRADATION

The characterization of NC presented in this section has been used for three manuscripts, all currently under review:

Shvedova, Anna A., et al., *Gender Differences in Murine Pulmonary Responses Elicited by Nano-Crystalline Cellulose,* Particle and Fibre Toxicology, under review.

This research paper established the pulmonary effects of NC exposure to mice, including oxidative stress, inflammation and damage to the lungs, as well as impaired pulmonary function. The findings also showed a significant increase in these effects for female mice as opposed to male. These results lead to the possible conclusion of increased risk of lung disease for females exposed to NC, consistent with other studies that suggest that sex hormones (such as estrogen) play an important role in the development of pulmonary diseases.

Author Contribution: PMF performed AFM image collection and statistical interpretation of collected images, as well as SEM and EDX characterization.

Menas, Autumn L. et al., *Evaluation of Nanocellulose Materials in Lung Epithelial Cells Revealed that Fibrillar Nanocellulose is Cytotoxic while Nanocellulose Crystals are Inflammogenic,* Journal of Environmental Science and Technology, under review.

This investigation explored differences in lung cell response between exposure to nanofibrillated cellulose (NCF) and nanocrystalline cellulose (CNC). It was shown that NCF exhibited greater cytotoxicity and produced lower cellular glutathione levels, evidence for oxidative stress. Alternatively, *in vitro* CNC exposure led to elevated levels of cytokines,

indicating an inflammatory response. The cytokine results showed similarities between NCF and carbon nanofibers, as well as between CNC and chitin.

Author Contribution: PMF performed AFM image collection and statistical interpretation of collected images, as well as DLS characterization. Data obtained through AFM and DLS studies allowed for the comparison of morphologies between different sources and forms of NC. The established differences in size and shape of the different NC samples were then related to disparities in response between the materials and lung epithelial cells. Microscopy analysis of carbon nanofiber and chitin (from sea shrimp shells) was also performed.

Yanamala, Naveena *et al., In vitro toxicity evaluation of (un)lignin-coated cellulose nanoparticles on human A549 and THP-1 cells,* Biomacromolecules, under review.

This article explored the difference in response of A549 and THP-1 lung cell monocultures to nanocrystalline (CNC) or nanofibrillated (CNF) cellulose, for both hydrophilic and lignin-coated (L-CNC or L-CNF) hydrophobic surface chemistries of nanocellulose. The report found little or no toxicity for A549 cells to any of the NC materials, while THP-1 cells showed a dose-dependent cytotoxic and inflammatory response, especially to CNC and L-CNF.

Author Contribution: PMF performed AFM and optical microscopy image collection and image analysis.

2.2.1 Methods and Materials

Transmission Electron Microscopy (TEM). TEM imaging was performed using an FEI Morgagni microscope operating at 80 keV. Samples were prepared by drying 5 µL of sample solution to a TEM grid (Electron Microscopy Sciences, Hatfield, PA), made of carbon film on a copper support (400 mesh). NC sample grids were subsequently stained by floating them (sample side down) on a 2% aqueous uranyl acetate solution for 30 min, followed by brief submersion in DI water. Analysis of the resulting images was performed using ImageJ.

Scanning Electron Microscopy (SEM) and Energy Dispersive X-ray Spectroscopy (EDX). SEM imaging and EDX analysis was performed using a Philips FEI XL-30 field-emission microscope, operating at 10.0 – 20.0 keV accelerating voltage. Samples were prepared by drying 5 µL of sample of solution on silicon wafer, which was pretreated by cleaning for 15 min in piranha solution (7:3 concentrated sulfuric acid:30% hydrogen peroxide, 60 °C).

Atomic Force Microscopy (AFM). AFM imaging was performed using a Multimode scanning probe microscope (Veeco) in tapping mode. The freshly-cleaved mica surface was functionalized with APTES by incubating the surface with 50 µL of 0.05% APTES aqueous solution for 1 min, followed by rinsing with NanoPure H_2O and drying with N_2 gas. The sample solution (5 µL) was then incubated on the surface for 2 min. After lightly dipping the mica in DI water, the mica was carefully dried with N_2 gas. An ACL probe (AppNano, Santa Clara, CA) was utilized at a frequency between 160-225 kHz, an amplitude set point between 1.5-1.8 V, and a minimized drive amplitude, generally between 100-300 mV. The resulting images were processed using Gwyddion software.

Dynamic Light Scattering (DLS). DLS analysis was performed on 1 g/L solutions using a Brookhaven Instrument Corporation ZetaPALS. 10 runs were averaged using a refractive index (real) of 1.474.

Reagents and Materials. All reagents were used as received without further purification. (3-aminopropyl)triethoxysilane (APTES) and 4-(2-hydroxyethyl)-1-piperazineethanesulfonic acid (HEPES) and was purchased from Sigma-Aldrich (St. Louis, MO). Nanocellulose samples were received from collaborators at the National Institute of Occupational Safety and Health (NIOSH, Morgantown, WV) and were originally sourced from Forest Products Laboratory (Madison, WI), American Process Inc. (Atlanta, GA) or Sigma-Aldrich.

Table 2. Nanocellulose labels

Label No.	Particles	Source	Manufactured Process
1	Cellulose Nanocrystals	Forest Products Laboratory	Freeze Dried Powder
2	Cellulose Nanocrystals	Forest Products Laboratory	10% wt Gel
3	Cellulose Nanocrystals	Forest Products Laboratory	Spray Dried Powder
4	Cellulose Nanocrystals	Forest Products Laboratory	Freeze Dried Powder
5	Cellulose Nanofibrils	Forest Products Laboratory	0.9% wt Gel
6	Cellulose Nanofibrils	Forest Products Laboratory	Freeze Dried Powder
7	AVAP CNC from Euca	American Process Inc	Spray Dried Powder
8	Euca AVAP L-CNC	American Process Inc	Spray Dried Powder
9	Euca AVAP CNF	American Process Inc	Spray Dried Powder
10	Euca AVAP L-CNF	American Process Inc	Spray Dried Powder
11	Microcrystalline Cellulose	Sigma Cat #	Powder

Table 2. Summary of NC labels, sources and manufacturing processes. Abbreviations: CNC (cellulose nanocrystals), AVAP (American value added pulping), CNF (carbon nanofibrils), L-CNC (lignin-coated CNC), L-CNF (lignin-coated CNF).

2.2.2 Nanocellulose Characterization: AFM, Optical Microscopy, and DLS
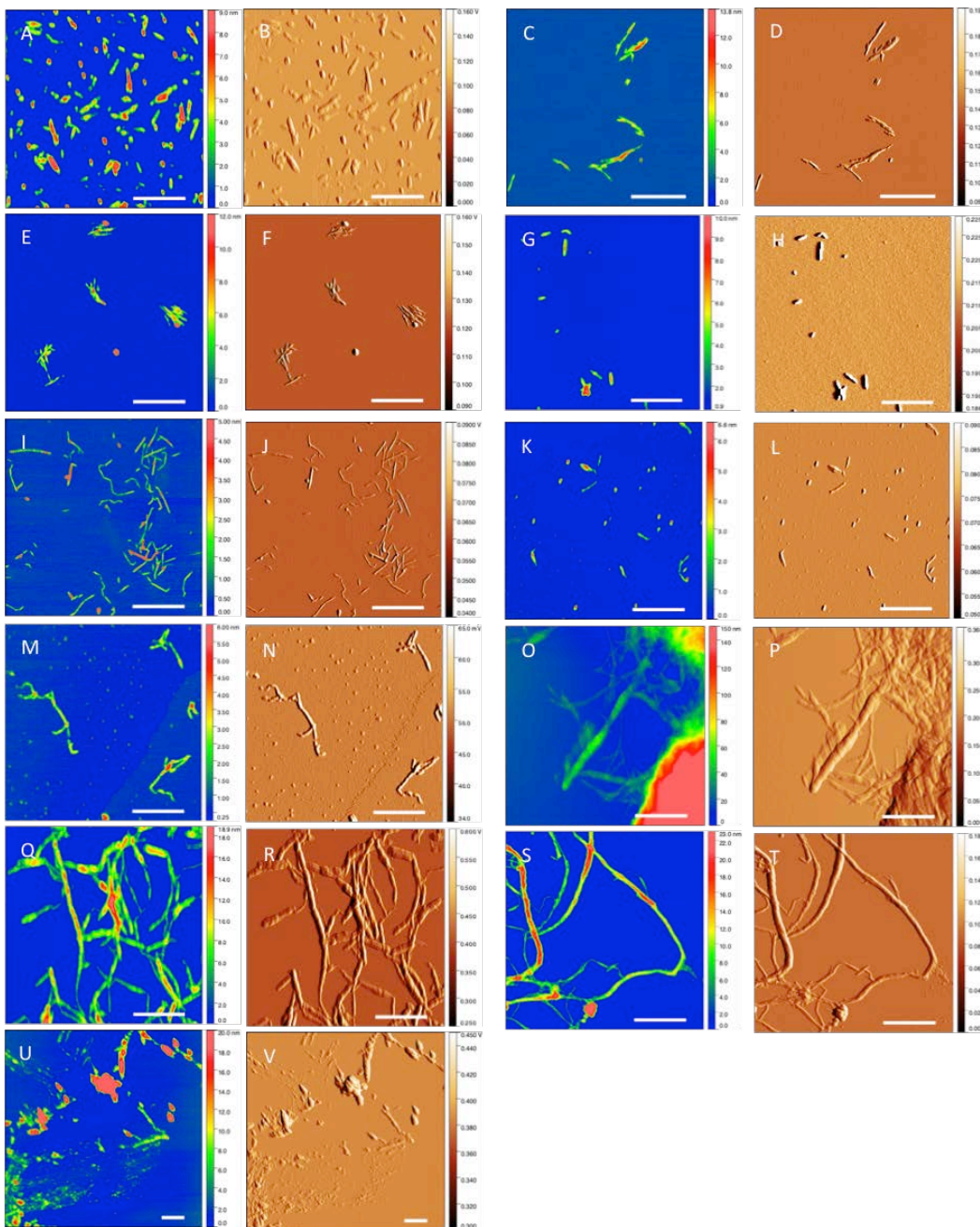
Figure 19: Nanocellulose - AFM characterizations

Figure 19. AFM height and amplitude images for nanocellulose samples 1 (A, B), 2 (C, D), 3 (E, F), 4 (G, H), 5 (I, J), 6 (K, L), 7 (M, N), 8 (O, P), 9 (Q, R), 10 (S, T), and 11 (U, V). Scale bar is 500 nm for all images.
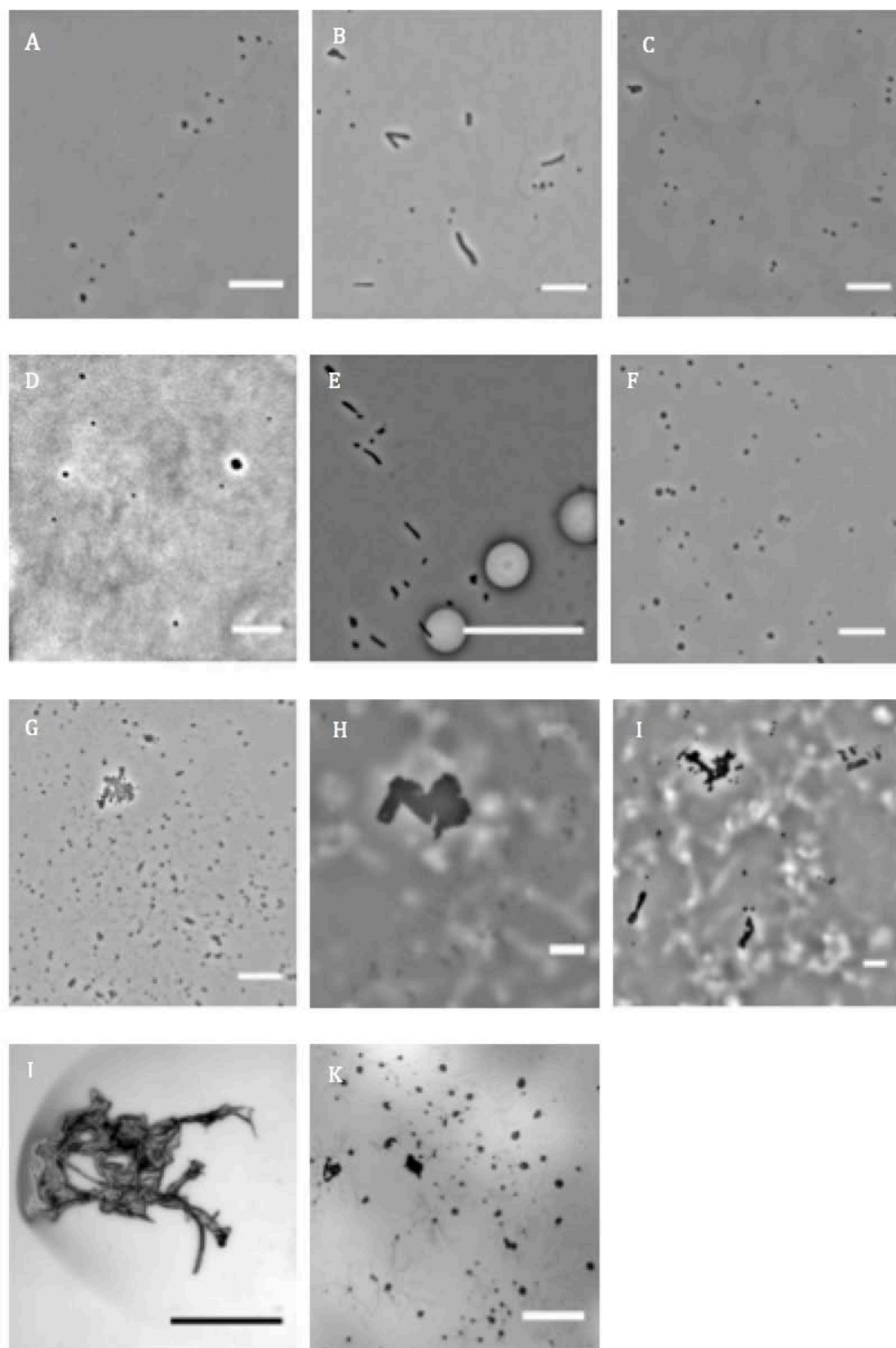
Figure 20: Nanocellulose - optical microscopy characterizations

Figure 20. Optical microscopy images for nanocellulose samples: 1 (A), 2 (B), 3 (C), 4 (D), 5 (E), 6 (F), 7 (G), 8 (H), 9 (I), 10 (J), and 11 (K). Scale bar is 50 µm for all images.

Sample	DLS		AFM		Optical	
	Effective diameter (nm)	Polydispersity	Length (nm)	Width (nm)	Area (µm²)	Diameter (µm)
1	149.8 ± 2.6	0.344 ± 0.009	158 ± 97	54 ± 17	-	-
2	137.5 ± 1.2	0.238 ± 0.008	209 ± 136	37 ± 15	-	-
3	96.6 ± 0.9	0.279 ± 0.008	104 ± 44	47 ± 11	-	-
4	138.6 ± 2.6	0.372 ± 0.007	144 ± 50	60 ± 14	-	-
5	214.2 ± 6.2	0.4 ± 0.01	-	20 ± 4	4.950 ± 2.818	2.393 ± 0.782
6	1904.3 ± 631.6	0.431 ± 0.074	142 ± 14	28 ± 11	9.271 ± 4.939	3.290 ± 1.005
7	37447.6 ± 19469.6	0.518 ± 0.079	-	37 ± 7	6.459 ± 5.850	2.524 ± 1.360
8	not soluble	not soluble	-	47 ± 9	22.770 ± 21.542	4.760 ± 2.598
9	158.2 ± 11.1	0.1 ± 0.044	-	56 ± 14	25.391 ± 9.943	5.561 ± 1.199
10	not soluble	not soluble	-	48 ± 20	1.726 ± 1.295	1.393 ± 0.520
11	23969.3 ± 10601.2	0.266 ± 0.095	-	95 ± 41	4.624 ± 4.417	2.105 ± 1.211

Table 3. Summary of NC DLS, AFM, and optical microscopy characterizations.

Representative AFM images of all nanocellulose samples (Fig. 19) confirm the nanocrystal or nanofibril architecture adopted by all samples except sample 11 (microcrystalline cellulose), which exhibited a more amorphous morphology. Analysis of AFM images allowed for the assessment of the length and width dimensions for the different NC samples. For all samples, the measured width was less than 100 nm, showing that the nanofibril architecture adopted by cellulose does indeed fall within the nanoscale domain. The width measurements are generally between 20 and 60 nm, with microcrystalline cellulose exhibiting a wider fibril width of close to 100 nm. When the entire NC structure was clearly differentiated in an image, the length of that particle could be evaluated. Unsurprisingly, most cellulose nanocrystals met this requirement, while most cellulose nanofibrils were either too long or too aggregated to be measured with confidence. Samples 8 and 10, which are lignin-treated cellulose nanocrystals and

nanofibrils, respectively, exhibited extreme aggregation, and individual particles could not be extracted by using any combination of sonication and solvents.

For those samples where the entire particle was not discernible, optical microscopy (Fig. 20) was useful to assess the aggregation characteristics. All samples formed micron-scale aggregates after drying on freshly-cleaved mica substrates. When individual nanoparticles could not be analyzed using AFM, the NC aggregates formed were evaluated based on their average area. This average area was then modeled as a circle to determine what the diameter of such a circle would be.

The use of DLS to describe the hydrodynamic radius of the NC samples helped to corroborate some of the AFM findings. However, the software used to make DLS size evaluations model the particle as a sphere. As shown with the AFM results, individual NC particles are either rod- or fibril-shaped. DLS effective diameter and AFM length measurements correlated well for samples 1-4, demonstrating that the hydrodynamic "shape" of the individual cellulose nanocrystals is at least roughly spherical. Cellulose nanofibrils may form architectures with interlaced networks of particles that likely move in solution as a single entity. The measured DLS effective diameter therefore pertains to these macrostructures as opposed to individual fibrils, and as such do not match with the size evaluations made using AFM. In addition, solvent-particle interactions could allow the fibril networks to relax and expand, which contrasts with the results seen for optical microscopy. Under dry conditions, the macroscale architectures may condense in an attempt to lower the surface energy inherent with nanostructures. Samples 8 and 10, which did not form stable colloidal solutions in water, could not be analyzed using DLS.

2.2.3 Enzymatic Degradation of Nanocellulose: NC-1 Characterizations

To investigate the effect of myeloperoxidase (MPO) and peroxide on NC, NC sample #1 (henceforth referred to as NC-1) was further characterized using SEM, EDX and TEM. The use of SEM allows for an additional approach to inspect the morphology, while EDX is useful in determining the chemical composition. Figure 21 shows representative SEM images and EDX spectra for NC-1. Micron-long aggregates are observed, with widths of roughly 300 nm. Nanofibrils can be seen extending off the larger microfibrils (Fig. 21b). The poor conduction of NC resulted in charging on the surface of the material and caused a deleterious effect on the quality of the images.
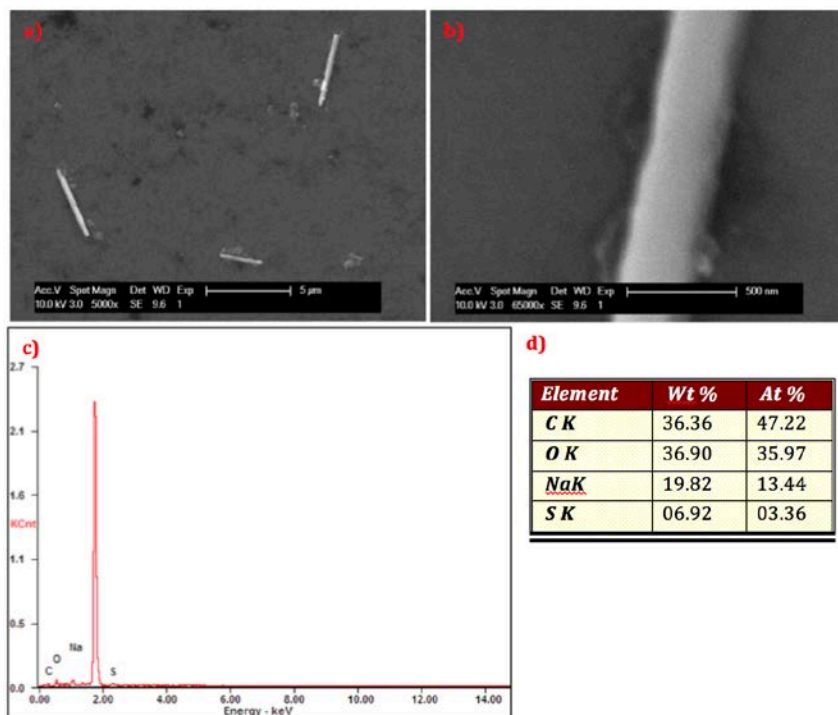

Figure 21: NC-1 - SEM and EDX characterization

Figure 21. SEM characterization of NC-1. Low-zoom (a) and high-zoom (b) images further reveal the micron-scale aggregation. The EDX spectrum (c) and corresponding elemental analysis table (d) shows the expected chemical composition of NC-1.

48

The EDX spectroscopy results of NC-1 exhibited the expected chemical make-up for the material. Pure cellulose, as show in Figure 7d, is composed of a 6:5 C:O atomic ratio, and the sulfuric acid hydrolysis treatment replaces some of the hydroxyl groups with sulfate esters. Sodium was added during the manufacture process and serves as a counter cation. The EDX spectra includes a large peak near 1.8 keV, which corresponds to the silicon peak that arises from the Si wafer substrate. The contribution of Si was removed from consideration when calculating the chemical composition.

The ease and quickness of observing relatively large sample areas makes TEM a useful technique for the assessment of NC morphology. While AFM provides additional information about the sample height, it is a low-throughput technique in that individual images take minutes to collect, in comparison to TEM which can produce images in seconds. By itself, however, NC is difficult to image with TEM, since the low density of the material and its chemical makeup of lighter elements result in relatively few electron scattering events and low image contrast. The use of uranyl acetate (UA) as a stain helps to provide image contrast and clarity of the edges of material, as the heavy uranium ions form a dark background on the grid surface. The utility of UA as a stain is exhibited in Figure 22, where unstained (22a) and stained (22b) samples are compared. Figure 22b shows that the individual NC nanocrystals become resolved and discernible after using a 30 min stain treatment of the dried sample on the TEM grid. Aggregation of the material is commonly observed, and could not be prevented. Functionalization and surface charging of the grid using poly-l-lysine, APTES, UV/O$_3$ and O$_2$ plasma treatments were all attempted in a effort to provide NC particle separation, to no avail.
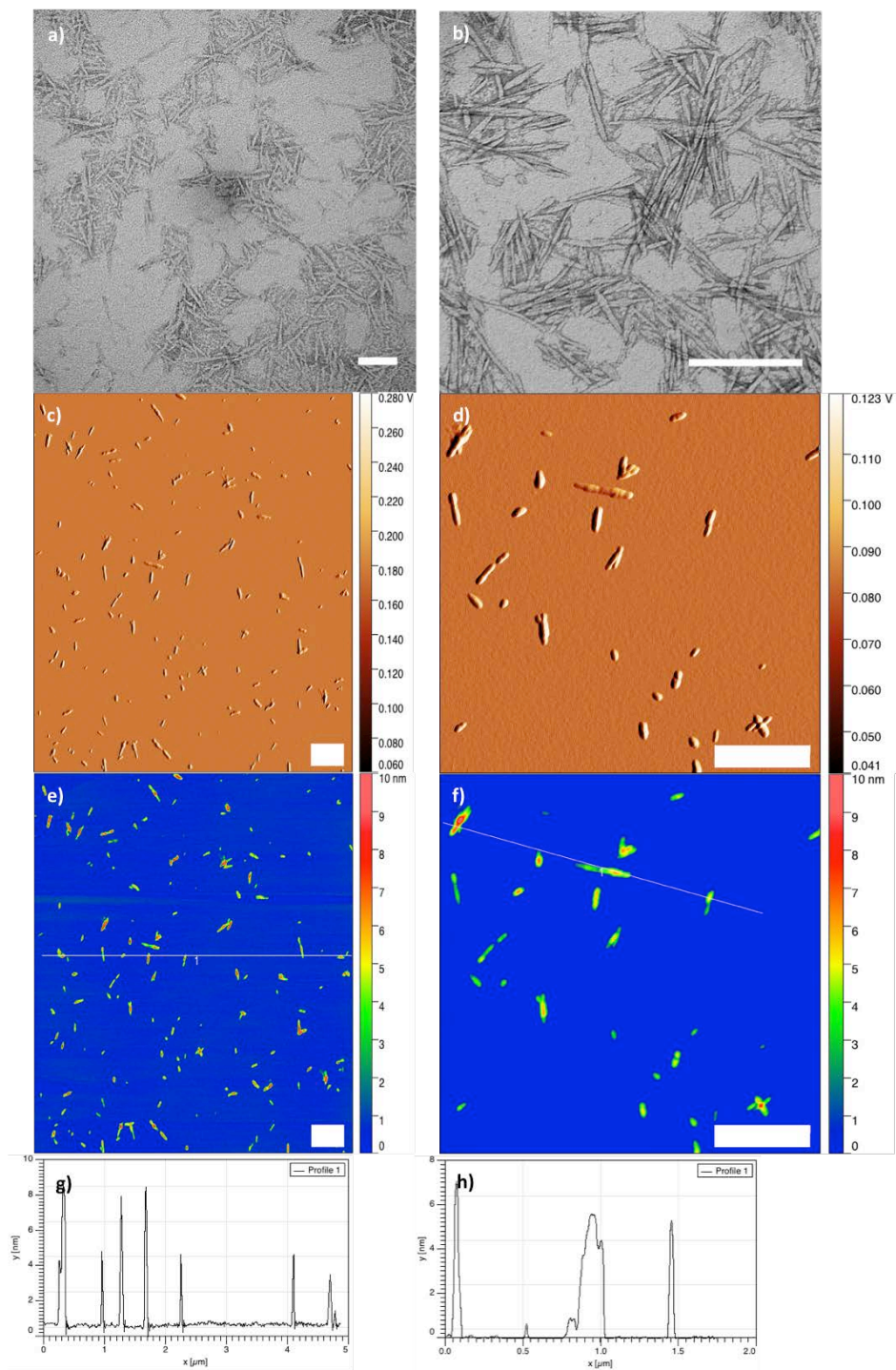
Figure 22: NC-1 - TEM and AFM characterization

Figure 22. TEM and AFM characterization of NC-1. TEM without (a) and with (b) UA stain treatment. Amplitude (c, d) and height (e, f) AFM of NC-1 in Nanopure H_2O. Profiles for lines given in (e) and (f) shown in (g) and (h), respectively. Scale bars: 200 nm (a, b), 500 nm (c-f).

50

2.2.4 Enzymatic Degradation of Nanocellulose: Experimental Design

The enzymatic degradation of NC-1 was performed by first preparing 20 mM HEPES buffer solution, which was adjusted to pH 7.4 using NaOH. NaCl was added to make the chloride concentration 48.6 mM. 18.75 mM H_2O_2 was prepared by mixing 9.6 µL stock H_2O_2 with 4.99 mL H_2O. Myeloperoxidase solution was prepared by dissolving 100 µg of MPO in 350 µL H_2O. The initial reaction solution contained 15 µL NC-1 (1 g/L), 30 µL MPO and 5 µL H_2O_2 in 1500 µL of HEPES buffer. Additions of 4 µL H_2O_2 were performed every 2 h for four times total every day. Daily additions of 30 µL MPO were made at the beginning of each day. These additions ensured that active MPO was present in solution for at least 8 h every day, and that the H_2O_2 concentration was kept below 5 mg/L at all times. The concentration of H_2O_2 was assessed by applying 5 µL of reaction solution to peroxide test strips. AFM samples were prepared on freshly cleaved mica that was functionalized using 0.05% APTES solution. The reaction solution was placed on an active shaker plate and kept in an incubator at 37.0 °C.

2.2.5 Enzymatic Degradation of Nanocellulose: Results

The degradation potential of MPO on NC-1 was assessed with AFM and TEM microscopy imaging. TEM characterization was initially hindered by interaction between the original buffer used (10 mM phosphate buffered saline, PBS) and the UA staining agent. Phosphate and uranium ions will combine upon drying to form amorphous crystals that prevented the uranium ions from homogeneously distributing across the surface of the grid. To alleviate this issue, HEPES buffer was used instead and produced useable results. Although aggregation was still apparent, approximately single-layer films of NC were capable of being

imaged on UA-treated carbon-film TEM grids, and NC nanocrystal edges became much clearer after applying the stain. TEM images of the initial reaction solution (both with and without MPO added), as well as   NC-1 after 1, 3, 6, and 9 days of incubation are shown in Figure 23.

The use APTES for mica surface functionalization allowed distinct NC nanocrystals to be observed using AFM for samples prior to the addition of MPO (Figure 24a). The improved separation between individual NC particles is immediately apparent when comparing Figures 23a and 24a. Functionalization of the mica using APTES creates a positively charged surface. In neutral aqueous solution, NC-1 is negatively charged (-68.26 ± 2.89 mV, determined using the zeta potential measurement capability of the DLS instrument) and will therefore spread out on the mica to maximize Coulombic attraction between the opposite charges. Since surface functionalization of the TEM grid was unsuccessful, aggregation of the material dominates during the drying process, as this helps to lower the enhanced surface energy inherent for most nanoscale architectures. However, the material displayed immense aggregation once MPO was mixed with NC-1, with very few (if any) individual nanocrystals discernible, as seen in Figure 24b. AFM imaging revealed that the NC-1/MPO mixture showed increased aggregation as the duration of incubation increased, as was seen for TEM.
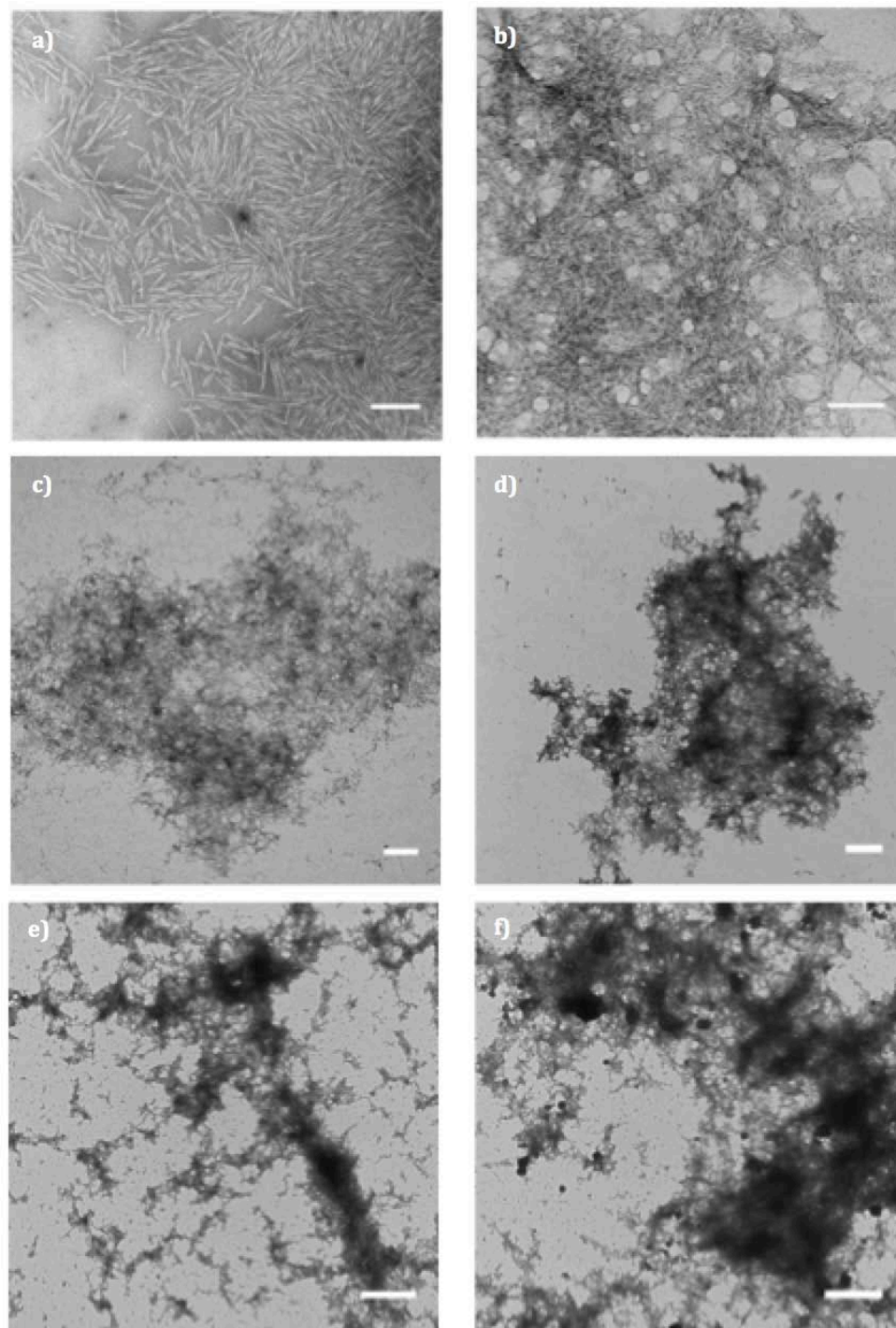
Figure 23: NC-1 - incubation with MPO TEM characterization

Figure 23. TEM characterization of NC-1 incubation with MPO. Pre-MPO addition (a, 200 nm), initial reaction solution (b, 200 nm), 1 d (c, 500 nm), 3 d (d, 1 µm), 6 d (e, 1 µm), and 9 d (f, 1 µm) incubation time. Scale bar lengths given in parentheses.
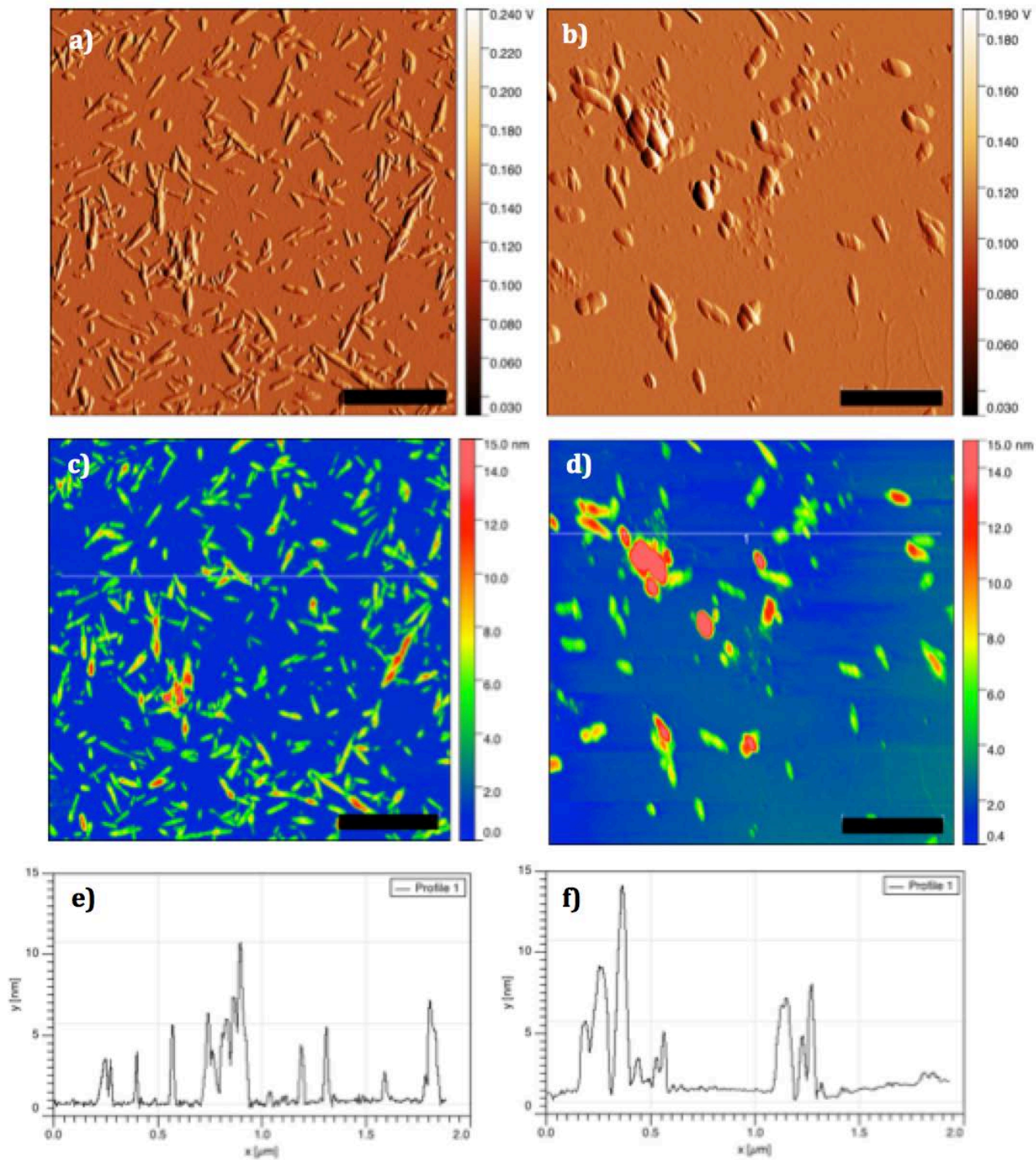
Figure 24: NC-1 - mixture with MPO AFM characterization

Figure 24. AFM amplitude (a, b), height (c, d) and profile (e, f) characterization of NC-1 with and without MPO. Pre-MPO addition (a, c, e), and with MPO (b, d, f). Scale bar is 500 nm for all images.
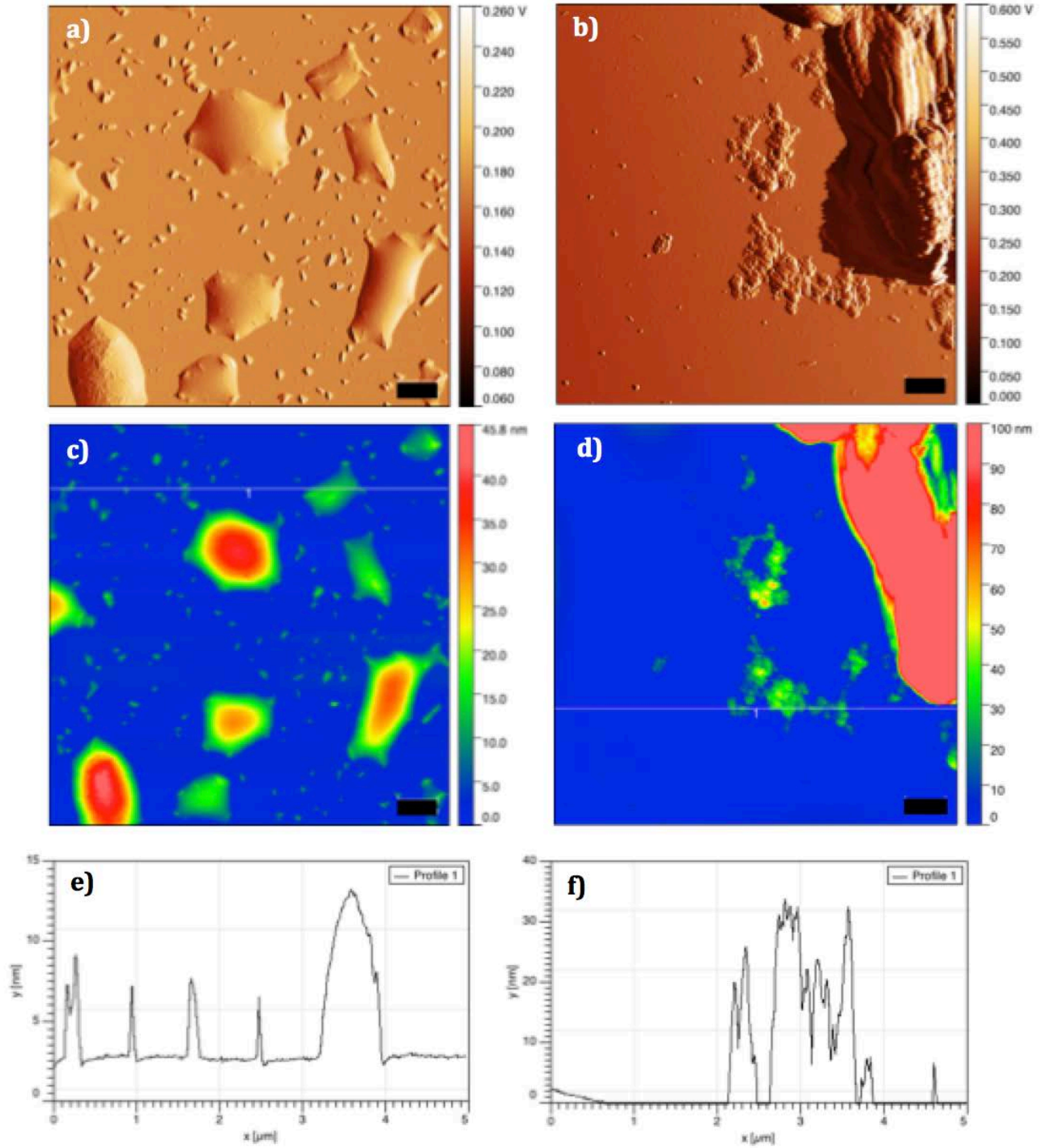
Figure 25: NC-1 - incubation with MPO AFM characterization

Figure 25. AFM amplitude (a, b), height (c, d) and profile (e, f) characterization of NC-1 after 2 and 6 d incubation with MPO. 2 d degradation (a, c, e), and 6 d degradation (b, d, f). Scale bar is 500 nm for all images.

2.2.6 Discussion

The addition of and incubation with MPO and H_2O_2 generates a few interesting consequences for NC-1. For one, the amount of aggregation, especially in the form of material stacking, greatly increases. Second, the emergence of discrete holes in the aggregates appears in TEM images. Direct (positive) staining of the NC-1/MPO also is observed for incubated samples, instead of the negative staining seen in Figure 22b and 23a.

The enzymatic degradation of NC-1 using MPO resulted in material aggregation when observed under AFM. While the initial material could be effectively separated by utilizing functionalization of the mica surface, the electrostatic interactions between negatively-charged NC-1 and positively-charged APTES were either nonexistent or not strong enough to separate individual crystals of the degraded material. Figure 25 shows the emergence of aggregates after 2 d of incubation, and after 6 d incubation observation of aggregates dominates. The presence of somewhat distinct, pseudo-spherical smaller structures in Figure 25b may be the product of individual NC crystals degrading, or possibly individual MPO domains. The favorable interaction between these degradation products over particle-solvent interactions may be the basis for the formation of the observed aggregation behavior.

AFM characterization of the starting and degraded materials mostly correlates with the TEM images. As shown in Figure 24a, NC-1 in HEPES buffer shows distinct morphology and particles can be easily distinguished. The addition of MPO (Figure 24b) leads to immediate aggregation of some material, while other nanocellulose structures remain separated. Height analysis of the pure NC-1 material (Figure 24c) shows that individual NC particles are approximately 4-6 nm thick, and areas where two particles are stacked are twice this thickness, roughly 10 nm. The aggregation areas found in MPO/NC-1 mixtures exhibited thicknesses

greater than 12 nm, showing that the enzyme was capable of associating with nanocellulose effectively.

While the incubation of NC-1 with MPO/H_2O_2 did not produce obvious degradation in the form of length or width decrease for the nanocrystal, the evolution of aggregates allows for a few possible conclusions to be considered. The formation of aggregates could possibly be the result of nanocellulose degradation followed by a subsequent clumping of degradation material around the remaining nanostructures. This aggregation may be a consequence of an increase in surface energy that can accompany a "shrinking" of the material through degradation. It is also possible that the aggregation behavior observed between NC-1 and MPO leads to the removal of NC-1 from a biological system (such as the lungs) through a different pathway than just by breaking down NC-1 into smaller and smaller fragments. Large scale aggregation of NC-1/MPO may allow the aggregates to be transported either out of the body (through coughing, for example) or to different organs, which could cause it to be subjected to other environments.

2.2.7   Conclusion

The incubation of NC-1 with MPO and H_2O_2 has been shown to result in increased aggregation of the materials over the course of a 9 day investigation. While the TEM and AFM analysis of the results did not show any apparent degradation of NC, the aggregation of these materials hindered the ability to assess the affect on individual nanocrystals. Further investigation of the NC-1/MPO interaction would benefit from the removal of MPO from the reaction system following incubation so that any change in the size of nanocrystals may be observed. Although notable degradation is not obvious, the aggregation of these materials upon mixing may still allow for the removal of NC-1 from a biological system.

2.3   HRP-DNA ORIGAMI INTERACTION WITH GRAPHENE OXIDE

2.3.1   Methods and Materials

Atomic Force Microscopy (AFM). AFM imaging was performed using a Multimode scanning probe microscope (Veeco) in tapping mode. An ACL probe (AppNano, Santa Clara, CA) was utilized at a frequency between 160-225 kHz, an amplitude set point between 1.5-1.8 V, and a minimized drive amplitude, generally between 100-300 mV. The resulting images were processed using Gwyddion software.

Reagents and Materials. All reagents were used as received without further purification. Graphene oxide in aqueous solution (5 mg/mL) was purchased from Graphene Supermarket. DNA origami with horseradish peroxidase samples were received from the Hao Yan group at Arizona State University (Tempe, AZ). NanoPure water (18.2 MΩ resistivity) was used.

2.3.2   Results

Preliminary characterization of the starting materials was performed to ensure the viability of exploring the use of DNA/HRP origami structures to localize the degradation of GO. As shown in Figure 26, individual DNA origami with well defined HRP, discrete GO sheets, and GO-DNA/HRP mixtures can be visualized. Figure 26e and 26f shows that the DNA/HRP architectures are still discernible even after mixing and that aggregation of the material is not a problem.
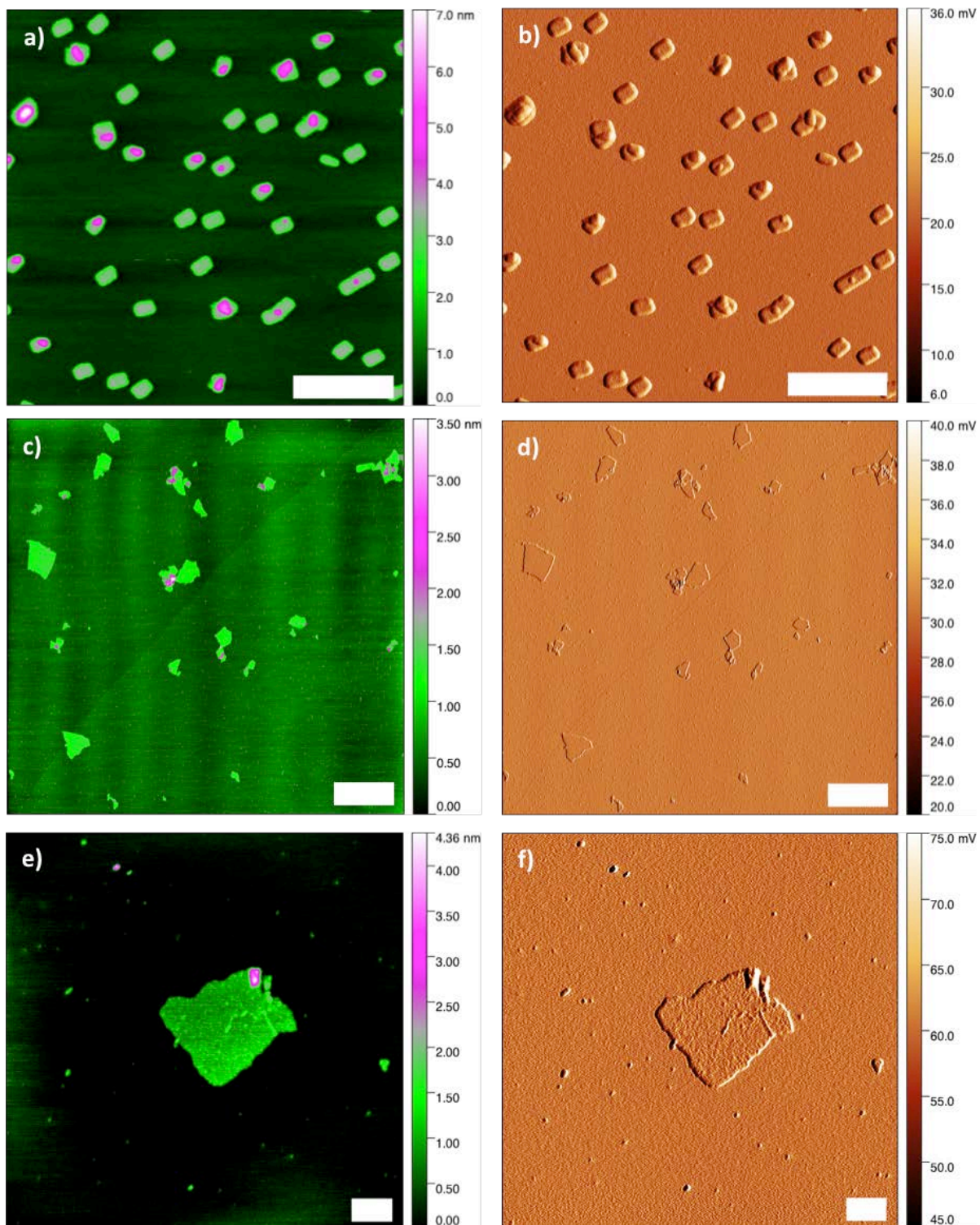
Figure 26: GO-HRP/DNA origami - AFM characterization

Figure 26. AFM height (a, c, e) and amplitude (b, d, f) images of HRP/DNA (a, b), GO (c, d) and GO-HRP/DNA (e, f). Scale bars are 500 nm (a, b), 2 µm (c, d) and 200 nm (e, f).

2.3.3 Discussion

The initial characterization of the starting materials reveals that the degradation of GO in the presence of DNA/HRP origami could be possibly investigated using AFM. The fact that the two separate components can be visualized both individually and together lends credence to the idea that any observed degradation may be related to the presence of HRP. The immobilization of HRP on the DNA origami could then be utilized to localize the degradation sites on the GO sheets to areas near the HRP. If the diffusivity of the oxidizing species produced *via* HRP is minimized, the GO sheets will be degraded only in areas adjacent to the DNA/HRP architecture.

To explore such degradation, it is necessary to incubate the GO-DNA/HRP mixture in an H_2O_2-containing buffer solution for at least 5 days before hole formation is observed. Such an investigation is not possible at this time with the current instrumentation available. Notably, a liquid-cell AFM specimen holder is necessary to subject the sample to the reaction solution. The images shown in Figure 26 were performed on mica which is taped to the specimen holder, which can not be submerged in the reaction solution without degrading the tape adhesive and contaminating the reaction solution. Once the correct instrumentation is obtained and configured, it is predicted that observation of the degradation of GO in the presence of DNA/HRP and H_2O_2 will be possible and a straight-forward endeavor.

2.4 CHARACTERIZATION OF NOVEL AND EMERGING CARBON NANOMATERIALS

2.4.1 Methods and Materials

Atomic Force Microscopy (AFM). AFM imaging was performed using a Multimode scanning probe microscope (Veeco) in tapping mode. An ACL probe (AppNano, Santa Clara, CA) was utilized at a frequency between 160-225 kHz, an amplitude set point between 1.5-1.8 V, and a minimized drive amplitude, generally between 100-300 mV. The resulting images were processed using Gwyddion software.

Transmission Electron Microscopy (TEM). TEM imaging was performed using an FEI Morgagni microscope operating at 80 keV. Samples were prepared by drying 5 µL of sample solution to a TEM grid (Electron Microscopy Sciences, Hatfield, PA), made of carbon film on a copper support (400 mesh). Staining of chitin TEM samples as performed by floating the grid (sample side down) on a 2% aqueous uranyl acetate solution for 30 min, followed by brief submersion in DI water. Analysis of the resulting images was performed using ImageJ.

Optical microscopy. An Olympus IX81 inverted system microscope was utilized for optical imaging. Samples were prepared by drop casting 5 µL of 20 mg/L sample solution on freshly-cleaved mica and allowed to dry under ambient conditions.

Reagents and Materials. All reagents were used as received without further purification. Carbon nanofiber and chitin samples were received from collaborators at the National Institute of Occupational Safety and Health (NIOSH, Morgantown, WV) and were originally sourced from Pyrograf Products, Inc. (Cedarville, OH, carbon nanofiber) and Sigma-Aldrich (St. Louis, MO, chitin from sea shrimp shells). Sodium dodecyl sulfate was purchased from Sigma-Aldrich.

2.4.2 Results

The characterization of vertically grown carbon nanofiber (VGCNF) and chitin samples was performed to assess, in conjunction with collaborators at NIOSH, if the exposure of these materials presents any increased risk of pulmonary health problems. The morphology of VGCNF and chitin was performed using optical microscopy, TEM and AFM, and these results are presented in Figure 27, along with relevant literature examples for comparison.

The fiber-like morphology of VGCNF was first revealed under optical microscopy, as seen in Figure 28. In aqueous solution, VGCNF quickly aggregates, forming micron-sized bundles visible by eye. Brief sonication was used to form temporary dispersed solutions, while minimizing any damaging effect sonication treatment might have on the fibers. To further encourage unbundling, stock solutions of VGCNF were also diluted and briefly sonicated in 1% sodium dodecyl sulfate (SDS) aqueous solution. Surfactants such as SDS are commonly employed for aqueous carbon nanotube solutions, and it was hypothesized that SDS could help improve the colloidal stability of VGCNF in water-based solvents. This hypothesis proved correct, and allowed for the production of TEM and AFM samples with discernible VGCNF structures.

The microscopy analysis of chitin was met with considerable challenge, specifically in the separation of the bulk material into the expected nanoscale architectures. The use of uranyl acetate staining in TEM sample preparation eventually led to the observation of regular, crystal-like structures. Although these structures were not readily apparent using AFM, stacked plate structures could be seen with individual plate heights of roughly 2 – 5 nm.
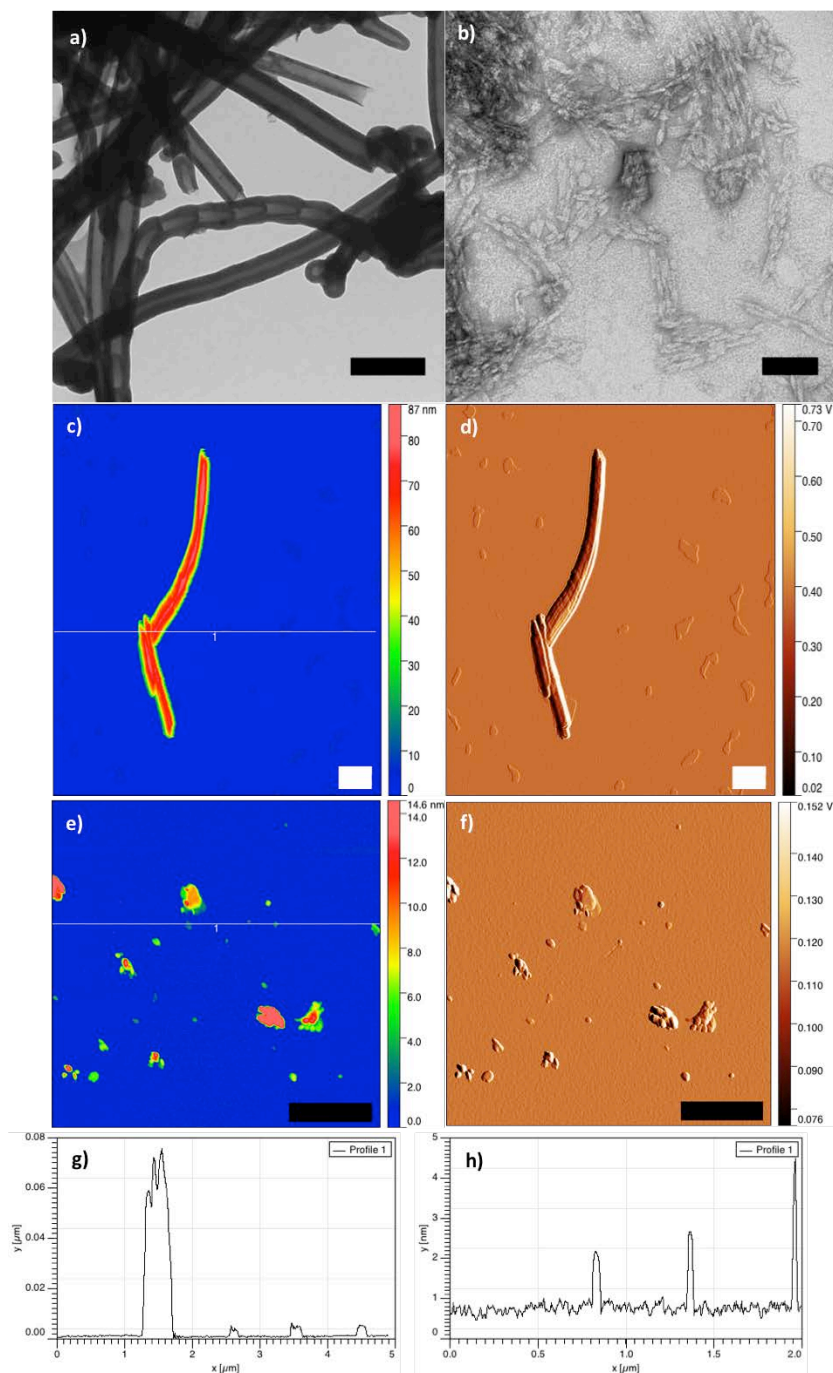
Figure 27: TEM and AFM imaging of carbon nanofiber and chitin

Figure 27. TEM (a, b) and AFM (c –f) characterization of VGCNF and chitin. a) VGCNF TEM, b) chitin TEM, c) VGCNF height AFM, d) VGCNF AFM amplitude, e) chitin height AFM, f) chitin AFM amplitude, g) profile for line drawn in (d), h) profile for line drawn in (e). Scale bars: a) 200 nm; b) 100 nm; c – f) 500 nm
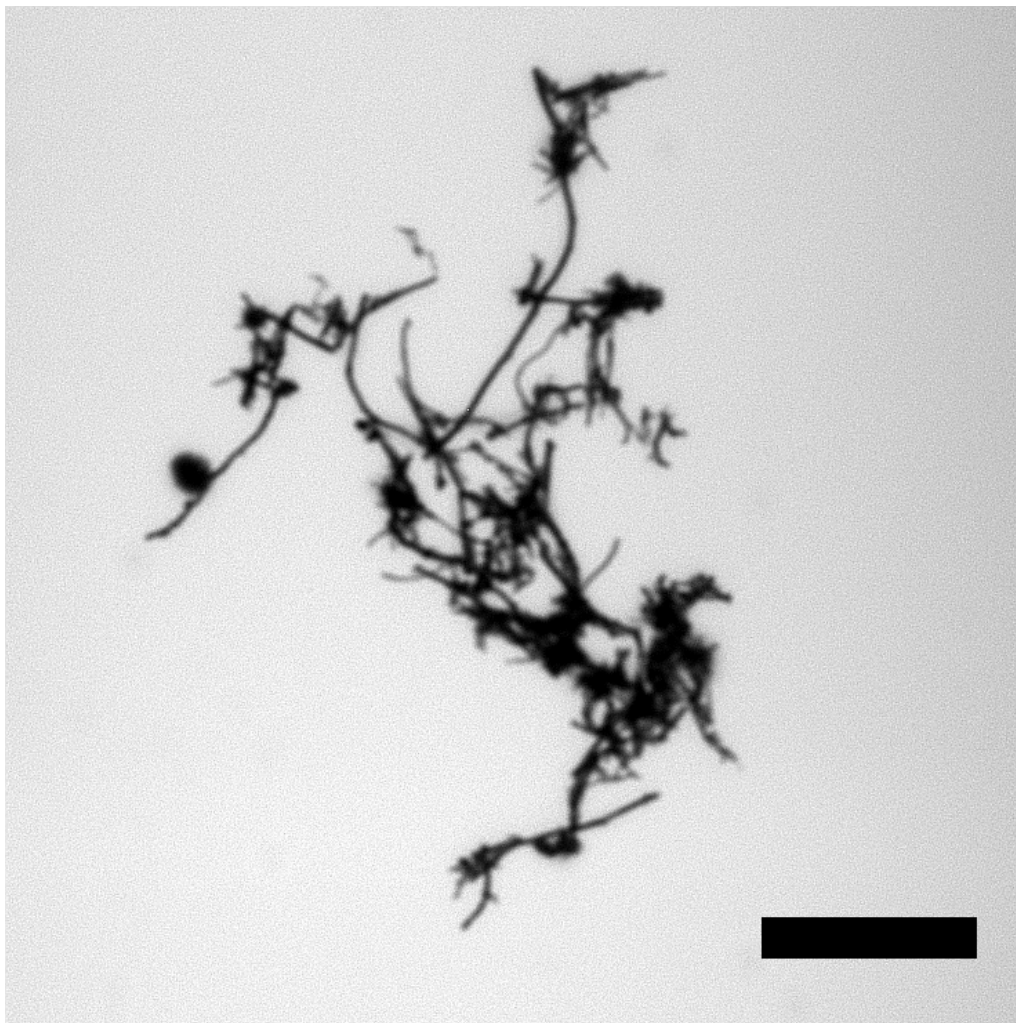
Figure 28: Carbon nanofiber optical microscopy image

Figure 28. Optical microscopy image of carbon nanofiber. Scale bar: 10 µm

2.4.3   Discussion

Qualitative microscopy analysis of TEM images of VGCNF revealed that the widths of individual fibrils fall in the nanoscale size regime, roughly 50 – 100 nm thick (Figure 27a). This thickness is further confirmed by AFM height imaging (Figure 27c), which shows that the height, and therefore the diameter, of an individual structure to be about 75 nm (figure 27g). Fiber thickness and width distributions were then quantitatively assessed using ImageJ. Analysis

of 34 different structures, observed using TEM, produced width and length distribution histograms shown in Figure 29. It was found that the width of the fibrils (84.2 ± 24.2 nm) was far more uniform than the length (2006.0 ± 1711.9 nm). The large standard deviation found for length measurements is evidence for the huge size distribution observed. The sample solution preparation, which included brief sonication to promote separation of fibril bundles, may have contributed to the presence of shortened fibrils that broke up upon sonication. This was an unavoidable consequence, however, as the fibrils were far too aggregated to measure without sonicating them. Furthermore, the average calculated size may have been further skewed toward shorter values, as only those fibrils which could be completely measured were considered. This population is limited by the viewing area of the microscope, and some fibrils were observed that were larger than could be measured.
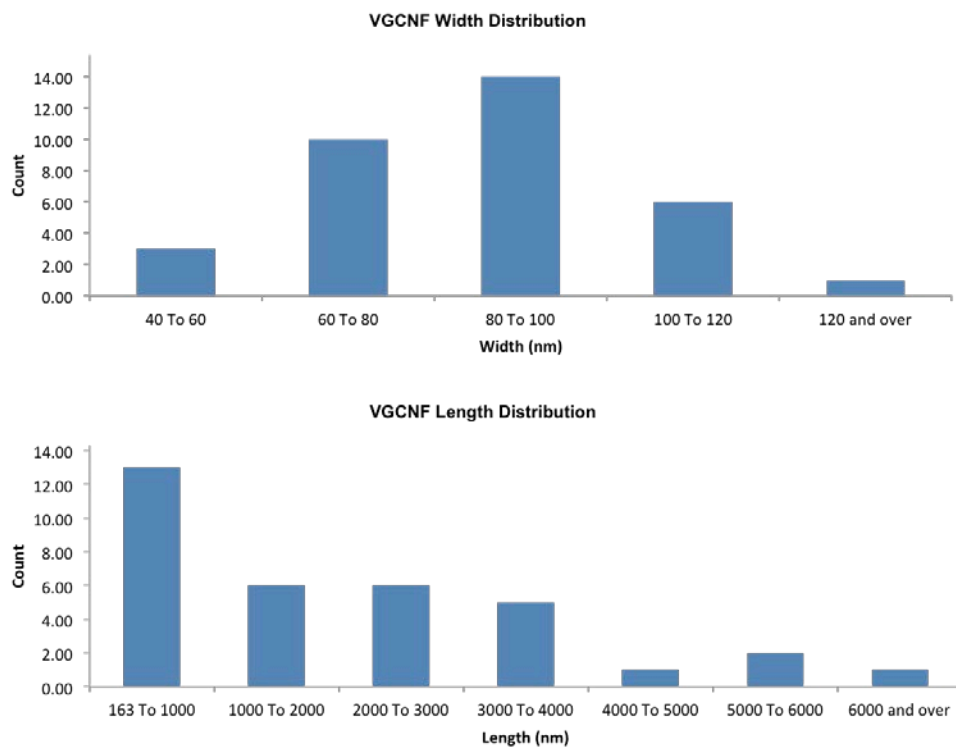
Figure 29: VGCNF width and length distribution histograms

Figure 29. Histograms showing the distribution of VGCNF widths and lengths.

Imaging of chitin revealed somewhat differing structures, depending on the technique used. For TEM, aggregates of distinct nanocrystals can be seen (Figure 27b), and the resolution was greatly enhanced through the use of uranyl acetate as a negative stain. Qualitative assessment of TEM micrographs shows nanocrystals with widths around 10 – 30 nm. The morphology of these structures appears to be somewhat plate- or fibril-like, although there is not much uniformity, and thus the lengths of individual structures are not easily discernible. For the evaluation of chitin nanoarchitecture morphology attributes, AFM imaging was utilized. Height analysis reveals individual plate structures with sub 1 – 2 nm heights (Figure 27h), while aggregates or stacks of these plates are somewhat larger but still mostly less than 10 nm.

Gwyddion software analysis of AFM images is useful for determining several morphological attributes of measured particles. Three of these attributes are minimum bounding size, maximum bounding size, and maximum inscribed disc diameter. The minimum and maximum bounding sizes dictate, respectively, the smallest 2-D gap a structure could fit through and the maximum 2-D gap a structure could fill up. These size evaluation only consider the architecture dimensions in the horizontal (basal) image plane. Similarly, the maximum inscribed disc diameter indicates the largest circle that could be placed inside the architecture in the horizontal plane.[53] It is fairly straightforward to imagine how these size attributes may determine interactions with a biological system on a purely physical level. For example, if the inscribed disc diameter is larger than the diameter of a pore found in an organ, the nanomaterial could potential clog that pore. Conversely, the minimum bounding size dictates whether or not that individual structure could pass through a pore of a given diameter. The results of analyzing 23 chitin structures found using AFM are summarized in Table 4.

Table 4. Chitin characterization summary

minimum bounding size (nm)	59.6 ± 44.01
maximum bounding size (nm)	85.4 ± 62.1
maximum inscribed disc diameter (nm)	46.3 ± 31.6

Table 4. Summary of chitin morphology properties determined from AFM imaging.

BIBLIOGRAPHY

1.   Geim, A.K. and K.S. Novoselov, *The rise of graphene.* Nat Mater, 2007. **6**(3): p. 183-191.
2.   Novoselov, K.S., et al., *Electric field effect in atomically thin carbon films.* Science, 2004. **306**(5696): p. 666-669.
3.   Lee, C., et al., *Measurement of the Elastic Properties and Intrinsic Strength of Monolayer Graphene.* Science, 2008. **321**(5887): p. 385-388.
4.   Kotchey, G.P., et al., *The Enzymatic Oxidation of Graphene Oxide.* ACS Nano, 2011. **5**(3): p. 2098-2108.
5.   Zhao, X., et al., *Flexible Holey Graphene Paper Electrodes with Enhanced Rate Capability for Energy Storage Applications.* ACS Nano, 2011. **5**(11): p. 8739-8749.
6.   Lin, Y., et al., *Bulk preparation of holey graphene via controlled catalytic oxidation.* Nanoscale, 2013. **5**(17): p. 7814-7824.
7.   Radich, J.G. and P.V. Kamat, *Making Graphene Holey. Gold-Nanoparticle-Mediated Hydroxyl Radical Attack on Reduced Graphene Oxide.* ACS Nano, 2013. **7**(6): p. 5546-5557.
8.   Hummers, W.S. and R.E. Offeman, *Preparation of Graphitic Oxide.* Journal of the American Chemical Society, 1958. **80**(6): p. 1339-1339.
9.   Bai, H., C. Li, and G. Shi, *Functional Composite Materials Based on Chemically Converted Graphene.* Advanced Materials, 2011. **23**(9): p. 1089-1115.
10.   Fenton, H.J.H., *LXXIII.-Oxidation of tartaric acid in presence of iron.* Journal of the Chemical Society, Transactions, 1894. **65**(0): p. 899-910.
11.   Venny, S. Gan, and H.K. Ng, *Modified Fenton oxidation of polycyclic aromatic hydrocarbon (PAH)-contaminated soils and the potential of bioremediation as post-treatment.* Science of The Total Environment, 2012. **419**: p. 240-249.
12.   Bauer, R. and H. Fallmann, *The Photo-Fenton Oxidation — A cheap and efficient wastewater treatment method.* Research on Chemical Intermediates, 1997. **23**(4): p. 341-354.
13.   McGillen, M.R., et al., *Is hydrogen abstraction an important pathway in the reaction of alkenes with the OH radical?* Physical Chemistry Chemical Physics, 2007. **9**(31): p. 4349-4356.
14.   Shao, P., et al., *Morphology-tunable ultrafine metal oxide nanostructures uniformly grown on graphene and their applications in the photo-Fenton system.* Nanoscale, 2015. **7**(34): p. 14254-14263.
15.   Guo, S., G. Zhang, and J.C. Yu, *Enhanced photo-Fenton degradation of rhodamine B using graphene oxide–amorphous FePO4 as effective and stable heterogeneous catalyst.* Journal of Colloid and Interface Science, 2015. **448**: p. 460-466.

16.	Bai, H., et al., *Insight into the Mechanism of Graphene Oxide Degradation via the Photo-Fenton Reaction.* The Journal of Physical Chemistry C, 2014. **118**(19): p. 10519-10529.

17.	Voinov, M.A., et al., *Surface-Mediated Production of Hydroxyl Radicals as a Mechanism of Iron Oxide Nanoparticle Biotoxicity.* Journal of the American Chemical Society, 2011. **133**(1): p. 35-41.

18.	Peng, G., et al., *In Situ Grown TiO2 Nanospindles Facilitate the Formation of Holey Reduced Graphene Oxide by Photodegradation.* ACS Applied Materials & Interfaces, 2016. **8**(11): p. 7403-7410.

19.	Edward, J.T., *Molecular volumes and the Stokes-Einstein equation.* Journal of Chemical Education, 1970. **47**(4): p. 261.

20.	Pabis, A., J. Szala-Bilnik, and D. Swiatla-Wojcik, *Molecular dynamics study of the hydration of the hydroxyl radical at body temperature.* Physical Chemistry Chemical Physics, 2011. **13**(20): p. 9458-9468.

21.	Pryor, W.A., *Oxy-Radicals and Related Species: Their Formation, Lifetimes, and Reactions.* Annual Review of Physiology, 1986. **48**(1): p. 657-667.

22.	Nelson, P., *Biological Physics: Energy, Information, Life*. 2004, New York: W.H. Freeman.

23.	He, F., et al., *The attachment of Fe3O4 nanoparticles to graphene oxide by covalent bonding.* Carbon, 2010. **48**(11): p. 3139-3144.

24.	Kotchey, G.P., et al., *A Natural Vanishing Act: The Enzyme-Catalyzed Degradation of Carbon Nanomaterials.* Accounts of Chemical Research, 2012. **45**(10): p. 1770-1781.

25.	Stone, K. and S. Ahmed, *Advances in Engineered Hemoproteins that Promote Biocatalysis.* Inorganics, 2016. **4**(2): p. 12.

26.	Degrand, C., et al., *Determination of horseradish peroxidase and a peroxidase-like iron porphyrin at a Nafion-modified electrode.* Analyst, 2001. **126**(6): p. 887-891.

27.	Seeman, N.C., *Nucleic acid junctions and lattices.* Journal of Theoretical Biology, 1982. **99**(2): p. 237-247.

28.	Rothemund, P.W.K., *Folding DNA to create nanoscale shapes and patterns.* Nature, 2006. **440**(7082): p. 297-302.

29.	Jiang, Q., et al., *DNA Origami as a Carrier for Circumvention of Drug Resistance.* Journal of the American Chemical Society, 2012. **134**(32): p. 13396-13403.

30.	Fu, J., et al., *Interenzyme Substrate Diffusion for an Enzyme Cascade Organized on Spatially Addressable DNA Nanostructures.* Journal of the American Chemical Society, 2012. **134**(12): p. 5516-5519.

31.	Moon, R.J., et al., *Cellulose nanomaterials review: structure, properties and nanocomposites.* Chemical Society Reviews, 2011. **40**(7): p. 3941-3994.

32.	Habibi, Y., L.A. Lucia, and O.J. Rojas, *Cellulose Nanocrystals: Chemistry, Self-Assembly, and Applications.* Chemical Reviews, 2010. **110**(6): p. 3479-3500.

33.	Roman, M., *Toxicity of Cellulose Nanocrystals: A Review.* Industrial Biotechnology, 2015. **11**(1): p. 25-33.

34.	Yanamala, N., et al., *In Vivo Evaluation of the Pulmonary Toxicity of Cellulose Nanocrystals: A Renewable and Sustainable Nanomaterial of the Future.* ACS Sustainable Chemistry & Engineering, 2014. **2**(7): p. 1691-1698.

35.	Kagan, V.E., et al., *Carbon nanotubes degraded by neutrophil myeloperoxidase induce less pulmonary inflammation.* Nat Nano, 2010. **5**(5): p. 354-359.

36. Al-Saleh, M.H. and U. Sundararaj, *A review of vapor grown carbon nanofiber/polymer conductive composites.* Carbon, 2009. **47**(1): p. 2-22.

37. Sherman, L.M. *Carbon Nanotubes Lots of Potential--If the Price Is Right*. [cited 2016 26 April].

38. Allen, B.L., P.D. Kichambare, and A. Star, *Synthesis, Characterization, and Manipulation of Nitrogen-Doped Carbon Nanotube Cups.* ACS Nano, 2008. **2**(9): p. 1914-1920.

39. Tibbetts, G.G., D.W. Gorkiewicz, and D.C. Hammond, *Apparatus for forming carbon fibers*. 1991, Google Patents.

40. Melechko, A.V., et al., *Vertically aligned carbon nanofibers and related structures: Controlled synthesis and directed assembly.* Journal of Applied Physics, 2005. **97**(4): p. 041301.

41. Nikolov, S., et al., *Revealing the Design Principles of High-Performance Biological Composites Using Ab initio and Multiscale Simulations: The Example of Lobster Cuticle.* Advanced Materials, 2010. **22**(4): p. 519-526.

42. Yan, N. and X. Chen, *Sustainability: Don't Waste Seafood.* Nature, 2015. **524**(7654): p. 3.

43. Ifuku, S. and H. Saimoto, *Chitin nanofibers: preparations, modifications, and applications.* Nanoscale, 2012. **4**(11): p. 3308-3318.

44. Peng, S., et al., *Synthesis and Stabilization of Monodisperse Fe Nanoparticles.* Journal of the American Chemical Society, 2006. **128**(33): p. 10676-10677.

45. Jia, T., et al., *A graphene dispersed CdS-MoS2 nanocrystal ensemble for cooperative photocatalytic hydrogen production from water.* Chemical Communications, 2014. **50**(10): p. 1185-1188.

46. Zhao, Y., et al., *A facile route to the synthesis copper oxide/reduced graphene oxide nanocomposites and electrochemical detection of catechol organic pollutant.* CrystEngComm, 2012. **14**(20): p. 6710-6719.

47. Pandey, J.K., et al., *Cellulose nanofiber assisted deposition of titanium dioxide on fluorine-doped tin oxide glass.* RSC Advances, 2014. **4**(2): p. 987-991.

48. Morton, K.C. and L.A. Baker, *Atomic force microscopy-based bioanalysis for the study of disease.* Analytical Methods, 2014. **6**(14): p. 4932-4955.

49. Zhang, J., et al., *Reduction of graphene oxide vial-ascorbic acid.* Chemical Communications, 2010. **46**(7): p. 1112-1114.

50. Zhu, M., et al., *Hydrothermal Synthesis of Hematite Nanoparticles and Their Electrochemical Properties.* The Journal of Physical Chemistry C, 2012. **116**(30): p. 16276-16285.

51. Suber, L., et al., *Effects of thermal treatments on structural and magnetic properties of acicular α-Fe2O3 nanoparticles.* Nanostructured Materials, 1999. **11**(6): p. 797-803.

52. McCoy, T.M., et al., *Noncovalent Magnetic Control and Reversible Recovery of Graphene Oxide Using Iron Oxide and Magnetic Surfactants.* ACS Applied Materials & Interfaces, 2015. **7**(3): p. 2124-2133.

53. Klapetek, P., D. Necas, and C. Anderson. *Gwyddion User Guide*. 2016 March 08 [cited 2016 May 04].